Diurnally Varying Ekman Layer in a Rossby Wave

ALAN SHAPIRO,[a] JASON CHIAPPA,[a] AND DAVID B. PARSONS[a]

[a] *School of Meteorology, University of Oklahoma, Norman, Oklahoma*

(Manuscript received 14 April 2023, in final form 4 December 2023, accepted 11 December 2023)

ABSTRACT: Weak but persistent synoptic-scale ascent may play a role in the initiation or maintenance of nocturnal convection over the central United States. An analytical model is used to explore the nocturnal low-level jets (NLLJ) and ascent that develop in an idealized diurnally varying frictional (Ekman) boundary layer in a neutrally stratified barotropic environment when the flow aloft is a zonally propagating Rossby wave. Steady-periodic solutions are obtained of the linearized Reynolds-averaged Boussinesq-approximated equations of motion on a beta plane with an eddy viscosity that is specified to increase abruptly at sunrise and decrease abruptly at sunset. Rayleigh damping terms are used to parameterize momentum loss due to radiation of inertia–gravity waves. The model-predicted vertical velocity is (approximately) proportional to the wavenumber and wave amplitude. There are two main modes of ascent in midlatitudes, an afternoon mode and a nocturnal mode. The latter arises as a gentle but persistent surge induced by the decrease of turbulence at sunset, the same mechanism that triggers inertial oscillations in the Blackadar theory of NLLJs. If the Rayleigh damping terms are omitted, the boundary layer depth becomes infinite at three critical latitudes, and the vertical velocity becomes infinite far above the ground at two of those latitudes. With the damping terms retained, the solution is well behaved. Peak daytime ascent in the model occurs progressively later in the afternoon at more southern locations (in the Northern Hemisphere) until the first (most northern) critical latitude is reached; south of that latitude the nocturnal mode is dominant.

KEYWORDS: Rossby waves; Vertical motion; Boundary layer; Diurnal effects; Ekman pumping; Differential equations

1. Introduction

Rossby waves are ubiquitous features of the atmosphere long known to produce oscillations of the westerly flow in the upper troposphere (e.g., Rossby 1939, 1940; Haurwitz 1940). Rossby waves owe their existence to gradients in potential vorticity (Hoskins et al. 1985). A basic review of Rossby wave dynamics can be found in Rhines (2002). Rossby wave packets are associated with extreme temperature, winds, and rainfall (e.g., Wirth et al. 2018), with the threat of these impacts potentially increasing with climate change (e.g., Kornhuber et al. 2020; Mann et al. 2018). The impact of Rossby waves on extreme precipitation is in part due to the poleward transport of water vapor (e.g., Grazzini et al. 2021), which can also generate ascent (e.g., Saffin et al. 2021).

Although synoptic-scale ascent in Rossby waves is typically weak, even a vertical velocity of 2 cm s^{-1}, if sustained for 10 h, would lift an air parcel over 700 m, a substantial fraction of the depth of a typical dry-convective atmospheric boundary layer (ABL) in the warm season. Such gentle but persistent ascent could play a role in initiating or maintaining convective systems. However, one key issue is "How would this ascent vary with the diurnal cycle of winds and stability in the atmospheric boundary layer?" Addressing this question may provide insight into why there is a nocturnal maximum in warm season precipitation over the central United States (Kincer 1916; Means 1952; Wallace 1975; Easterling and Robinson 1985; Dai et al. 1999; Carbone and Tuttle 2008). Although nocturnal convection in the central United States is often associated with the eastward propagation of an envelope of dissipating and regenerating mesoscale convective systems that originated over higher terrain to the west during the previous afternoon (Dai et al. 1999; Carbone and Tuttle 2008), it can also develop without an obvious connection to pre-existing convection, and may be associated with weak but long-lived ascent (Weckwerth and Parsons 2006; Wilson and Roberts 2006; Reif and Bluestein 2017; Trier et al. 2017; Shapiro et al. 2018; Gebauer et al. 2018). These studies have focused on convective systems during the warm season, often in the absence of strong surface cold fronts, but in flow patterns that can include Rossby waves.

In this study, we introduce an analytical model to explore the timing, strength, and patterns of ascent/subsidence and nocturnal low-level jets (NLLJ) in a diurnally varying frictional (viscous) boundary layer when the flow aloft is a zonally propagating Rossby wave. As the case where the environment is stably stratified (with differential vertical motion generating horizontal temperature gradients) appears to be analytically intractable, we restrict attention to neutrally stratified flows without horizontal temperature contrasts. We thus focus on the first part (diurnal wind cycle) of the issue noted above. The flow in our model is temporally and spatially periodic with the period and wavelength of the Rossby wave. Diurnal variations in turbulence associated with the morning and evening boundary layer transitions (Stull 1988) are simply (crudely) accounted for by explicitly specifying a diurnally periodic height-independent eddy viscosity. Our model thus combines the main aspects of the classical Ekman (1905) and Åkerblom (1908) theories for frictional oceanic and atmospheric boundary layers, the Blackadar (1957) theory for NLLJs arising from inertial oscillations triggered by the cessation of dry-convective turbulence at sunset, and the Rossby (1939) theory for the motion of meanders of the jet stream. The model provides a convenient framework to

Corresponding author: Alan Shapiro, ashapiro@ou.edu

DOI: 10.1175/JAS-D-23-0070.1

explore flow dependencies on Rossby wave characteristics, latitude, time of sunset, and day and nighttime levels of turbulence intensity. However, because of its simplistic treatment of boundary layer processes and lack of thermal stratification and baroclinicity, the model should not be used for more than a qualitative view of the flow in real ABLs.

For the simpler case where the flow is horizontally uniform and the pressure gradient force is temporally constant (no Rossby wave), Blackadar (1957) proposed that the shutdown of turbulence at sunset would trigger an inertial oscillation (IO) of the ageostrophic wind, with a wind speed maximum attained when the ageostrophic wind (which rotates anticyclonically around the geostrophic wind on a hodograph diagram) aligns with the geostrophic wind. In the Blackadar theory, a strong NLLJ develops from initial (sunset) wind and geostrophic wind profiles for which the ageostrophic wind is strong. This typically occurs near Earth's surface, where the winds are reduced from their free-atmosphere values which are often nearly geostrophic. A major role in the development of some NLLJs has been attributed to this mechanism (Parish et al. 1988; Zhong et al. 1996; Banta et al. 2002; Baas et al. 2009; Kallistratova and Kouznetsov 2012; Parish 2016, 2017; Parish and Clark 2017; Parish et al. 2020). Horizontal convergence of NLLJ winds likely contributes to the above-noted nocturnal maximum in warm season precipitation over the central United States (Pitchford and London 1962; Bonner 1966; Bonner et al. 1968; Maddox 1983; Trier and Parsons 1993; Walters and Winkler 2001; Tuttle and Davis 2006; Reif and Bluestein 2017; Shapiro et al. 2018; Gebauer et al. 2018; Weckwerth et al. 2019). Although NLLJ-associated convergence in this region is often found along the (usually northern) terminus of the NLLJ or where the NLLJ intersects a boundary layer convergence line, convergence can also arise on the lateral flanks of NLLJs from mechanisms that are less well understood.

In a study of a viscous version of the Blackadar model, Buajitti and Blackadar (1957) attributed the greater amplitude of their model wind speed oscillation at 30°N (versus 55°N) to the fact that the inertial frequency and diurnal frequency were equal at 30°N, but noted that, in their numerical experiments, "the tendency for resonance is actually not excessive because a large amount of viscous damping is characteristic of these layers" (p. 498) The theoretical studies of Paegle and Rasch (1973), Tan and Farahani (1998), Shibuya et al. (2014), Ingel' (2015), and Momen and Bou-Zeid (2017) also suggested that IOs in the ABL could exhibit resonant amplification at critical latitudes of 30°N or 30°S (or near such latitudes if the inertial frequency is based on absolute vorticity instead of planetary vorticity). However, the extent to which resonance impacts real atmospheric flows is relatively unexplored and unclear. Walters et al. (2008) point out disagreements between climatological analyses on the location of the southerly jet frequency maximum over the Great Plains, with the 2-yr study of Bonner (1968) placing the maximum near the Kansas–Oklahoma border, some ~7° north of 30°N, and the more extensive (40 years) study of Walters et al. (2008) putting the maximum in southern Texas, much closer to 30°N. However, the Walters et al. (2008) study also showed that, for subclasses of strong jets, the latitudes of peak jet frequency were closer to those indicated in the Bonner (1968) study.

The issue of resonance has been explored in more detail in the oceanographic literature. It has been suggested that upper-ocean Ekman layers in coastal waters forced by diurnally varying wind stresses associated with the land- and sea-breeze cycle, may display resonant responses near 30°N or 30°S (e.g., Shaffer 1972; Craig 1989; Simpson et al. 2002; Stockwell et al. 2004; Zhang et al. 2009, 2010; Hyder et al. 2011; Kim and Crawford 2014; Mihanović et al. 2016; Ashkenazy 2017; Vincze et al. 2019; Fearon et al. 2020). The most compelling evidence for diurnal-inertial resonance in a geophysical setting comes from some of these wind-driven Ekman layer studies. For example, working with the MITgcm general circulation model under periodic wind stress forcing, Ashkenazy (2017) found that the mean kinetic energy, upper-ocean current speed, and mixing layer depth were much larger in the simulation with the Coriolis frequency evaluated at 30°N than in simulations with Coriolis frequencies corresponding to other latitudes. Using the ROMS3 ocean model, Zhang et al. (2010) found that sea-breeze-driven upper-ocean currents in the Gulf of Mexico were much stronger and vertically extensive at the latitude reported closest to 30°N (29.7°N, northern Gulf) than at latitudes farther south in the Gulf. In an observational study using surface wind and ocean current data off the west coast of the United States, Kim and Crawford (2014) found that diurnal wind-current responses near 30°N were an order of magnitude larger than at other latitudes. Additionally, in laboratory experiments with a large rotating water tank configured with an oscillating horizontal plate used to simulate a periodic wind stress, Vincze et al. (2019) found that the Ekman depth and current speed were much larger when the oscillating plate frequency matched the Coriolis frequency.

Shapiro et al. (2018) proposed that the shutdown of turbulence at sunset, the trigger for a nocturnal IO/NLLJ in the Blackadar theory, can also trigger a weak but long-lived surge of convergent flow and ascent in the presence of a broad surface-based warm tongue. The governing equations in Shapiro et al. (2018) were the linearized Boussinesq equations of motion, thermal energy, and mass conservation for an inviscid stably stratified fluid on an f plane. The flow was described over one night as the solution to an initial value problem in which the initial (sunset) state was horizontally nondivergent and satisfied a zero-order jump model of a convective boundary layer. The resulting postsunset surge had aspects of an inertia–gravity wave response, with the (downward) propagation of phase lines indicating energy transfer away from the surface, and the zone of peak ascent gradually descending over the center of the warm tongue. Shapiro et al. (2018) also examined a simpler problem in which there was no warm tongue, but the free-atmosphere wind varied zonally as a stationary wave. Although the ascent in this second problem was much weaker than in the first problem, some of the weakness was likely due to the choice of parameter values. Specifically, with the southerly free-atmosphere geostrophic wind set to a small value (5 m s^{-1}) and the initial southerly boundary layer wind set to a large fraction (80%) of that value, the initial ageostrophic wind was weak

throughout the boundary layer, and would not be expected to generate a strong Blackadar-like IO/NLLJ or a strong initial surge. Stronger ageostrophic winds would presumably be attained with late afternoon winds that decreased on approach to the ground, as in the real atmosphere (or in a viscous model). Our present study is more closely related to this second problem, but differs from it in several important aspects. While the second model in Shapiro et al. (2018) was inviscid, limited to nighttime hours, stably stratified, and had a free-atmosphere wind in the form of a stationary geostrophically balanced wave, the present model is viscous (diurnally varying eddy viscosity), extends over multiple days and nights, is neutrally stratified (a major limitation), and has a free atmosphere wind that propagates as a Rossby wave.

The paper is arranged as follows. In section 2, we introduce the governing equations for the steady-periodic Ekman-Rossby problem (viscous problem) in which the eddy viscosity is diurnally periodic but otherwise temporally unrestricted. The simpler inviscid problem (limited to the nighttime) is solved in section 3. The viscous problem is solved in section 4. The derivations in sections 3 and 4 are fairly technical, but readers not interested in the details can safely skip them. Model resonance is explored in section 5. In section 6, the viscous solution is adapted to the case where the eddy viscosity varies as a piecewise constant function of time, with an abrupt increase at sunrise and an abrupt decrease at sunset. Examples of this latter flow type are presented in section 7. A summary and conclusions follow in section 8.

2. Formulating the steady-periodic Ekman-Rossby problem

A Rossby wave is propagating zonally on a uniform westerly current of strength U (>0) over the (flat) ground. The atmosphere is neutrally stratified and there are no horizontal temperature contrasts. Attention is restricted to the linearized steady-periodic state of laterally periodic flows on a beta plane. The flows are described in a Cartesian coordinate system in which x points east, y points north, and z is height above the ground. The corresponding velocity components are denoted by $u = u(x, z, t)$, $v = v(x, z, t)$, and $w = w(x, z, t)$ (t is time), respectively. Although these components are treated as two-dimensional (x, z), there will be a slight parametric dependence on y through the latitude in the Coriolis parameter. The remote ($z \to \infty$) velocity components are denoted by $u_\infty \equiv \lim_{z\to\infty} u$, $v_\infty \equiv \lim_{z\to\infty} v$, and $w_\infty \equiv \lim_{z\to\infty} w$. A complete list of symbols is provided in Table A1.

a. Governing equations

The governing equations are the linearized Boussinesq-approximated Reynolds-averaged equations of motion, with the horizontal part of the turbulent flux divergence neglected,

$$\frac{\partial u}{\partial t} + U\frac{\partial u}{\partial x} = fv - \frac{\partial \Pi}{\partial x} + K(t)\frac{\partial^2 u}{\partial z^2} - R(u - u_\infty), \tag{1}$$

$$\frac{\partial v}{\partial t} + U\frac{\partial v}{\partial x} = -fu - \frac{\partial \Pi}{\partial y} + K(t)\frac{\partial^2 v}{\partial z^2} - R(v - v_\infty), \tag{2}$$

the incompressibility condition,

$$\frac{\partial u}{\partial x} + \frac{\partial w}{\partial z} = 0, \tag{3}$$

and the hydrostatic equation. Here, $\Pi \equiv (p - p_r)/\rho_r$ is the kinematic pressure perturbation [$p = p(x, y, z, t)$ is pressure, $p_r = p_r(z)$ is pressure in a motionless and horizontally homogeneous reference atmosphere, ρ_r is a constant reference density]. Since the motion is hydrostatic with no horizontal temperature contrasts (as in the reference state), $\partial p/\partial z = dp_r/dz$, so $\partial\Pi/\partial z = 0$, and we can write $\Pi = \Pi(x, y, t)$. The eddy viscosity $K(t)$ is a specified diurnally periodic function of time. The constant R is a reciprocal time scale for Rayleigh damping that will be discussed below. The Coriolis parameter $f \equiv 2\Omega\sin\phi$ (ϕ is latitude, Ω is angular velocity of Earth) is considered within the beta plane approximation (Pedlosky 1987): f is constant unless it is differentiated with respect to y, in which case df/dy is constant. The latter is the Rossby parameter,

$$\beta \equiv \frac{df}{dy} = \frac{2\Omega\cos\phi}{a}, \tag{4}$$

where a is the mean radius of Earth.

For simplicity, K is taken to be independent of height. Although observations in Ekman layers show that an assumed height independence for K is an oversimplification, there appear to be a variety of case-dependent behaviors (e.g., K increasing or decreasing with height, displaying multiple extrema), with no general agreement on what the height dependence actually is (O'Brien 1970; Agee et al. 1973; Jeričević and Večenaj 2009; Constantin and Johnson 2019). However, Constantin and Johnson (2019) found that large variations in K with height do not necessarily translate into large differences in the boundary layer winds: "Most importantly, we have shown, for any eddy viscosity that is bounded and tends to a constant finite value at high altitude, that the decay and spiralling of the flow upward is an enduring property … The overall picture of the classical Ekman spiral is unaltered by the details of the varying eddy viscosity, which is slightly surprising. We might have expected that viscosity profiles with a number of local maxima and minima, for example, would produce a significant distortion of the familiar structure of the flow; this is not the case" (p. 412). This conclusion may explain why geophysical models sometime produce qualitatively reasonable results using an assumed constant K. For example, Maas and van Haren (1987) found that a constant-K model led to a good description of North Sea current profiles at the dominant tidal frequencies; a decay of current speed with depth via a constant-K Ekman spiral has been observed in upper-ocean currents (e.g., Hunkins 1966; Weller 1981; Price et al. 1987; Chereskin 1995; Price and Sundermeyer 1999); atmospheric Ekman flows consistent with a constant K were observed in polar regions during the summer by Grachev et al. (2005) and Rysman et al. (2016); constant-K models have provided a good description of slope flows at night and a reasonable approximation of slope flows during the day (e.g., Defant 1949; Tyson 1968; Papadopoulos et al. 1997; Oerlemans 1998);

Shapiro et al. (2022) found good agreement between the winds in a constant-K model of a baroclinic NLLJ over the Great Plains and lidar data.

The Rayleigh damping terms $-R(u-u_\infty)$ and $-R(v-v_\infty)$ in (1) and (2) are similar to terms included in slab and one-dimensional models of wind-driven Ekman layers in the upper ocean (e.g., Pollard and Millard 1970; Kundu 1976; Weller 1982; D'Asaro 1985; D'Asaro et al. 1995; Watanabe and Hibiya 2002; McWilliams and Huckle 2006; McWilliams et al. 2009; Park et al. 2009; Whitt and Thomas 2015; Gough et al. 2016; Jing et al. 2017). Weller (1982) and McWilliams et al. (2009) described the Rayleigh damping constant R as a parameterization of the momentum damping rate for upper-ocean currents due to the radiation of inertia–gravity waves to the deep ocean. As inertia–gravity waves could not be explicitly simulated in those models, the momentum damping rate associated with them could only be parameterized; inclusion of Rayleigh damping terms with time scales R^{-1} estimated from observations led to much improved predictions of current speeds. As inertia–gravity waves are ubiquitous in the atmosphere and can originate from the ABL (Shibuya et al. 2014; Jia et al. 2019) but cannot be simulated by our neutrally stratified model, we have included the damping terms. As we will see, Rayleigh damping precludes the development of resonant singularities in our model.

b. Boundary and temporal periodicity conditions

At the lower boundary, the flow satisfies the no-slip condition,

$$u|_{z=0}=0, \quad v|_{z=0}=0, \tag{5}$$

and the impermeability condition,

$$w|_{z=0}=0. \tag{6}$$

For lateral conditions, we consider the flow to be periodic in x with wavelength L,

$$u|_{x=0}=u|_{x=L}, \quad v|_{x=0}=v|_{x=L}. \tag{7}$$

The remote ($z\to\infty$) flow is a horizontally nondivergent barotropic Rossby wave superimposed on a uniform westerly current. This remote flow must be compatible with the forms of (1) and (2) as $z\to\infty$, where the turbulent stress and momentum damping terms vanish:

$$\frac{\partial u_\infty}{\partial t}+U\frac{\partial u_\infty}{\partial x}=-\frac{\partial \Pi}{\partial x}+fv_\infty, \tag{8}$$

$$\frac{\partial v_\infty}{\partial t}+U\frac{\partial v_\infty}{\partial x}=-\frac{\partial \Pi}{\partial y}-fu_\infty. \tag{9}$$

Taking $\partial/\partial x$[(9)] minus $\partial/\partial y$[(8)] yields the remote vorticity equation:

$$\frac{\partial \zeta_\infty}{\partial t}+U\frac{\partial \zeta_\infty}{\partial x}=-\beta v_\infty, \tag{10}$$

where $\zeta_\infty\equiv\partial v_\infty/\partial x-\partial u_\infty/\partial y=\partial v_\infty/\partial x$ is the remote vertical vorticity. Since the remote flow is horizontally nondivergent, a streamfunction ψ_∞ exists for which $u_\infty=-\partial\psi_\infty/\partial y$ and $v_\infty=\partial\psi_\infty/\partial x$. In terms of ψ_∞, (10) becomes

$$\left(\frac{\partial}{\partial t}+U\frac{\partial}{\partial x}\right)\frac{\partial^2\psi_\infty}{\partial x^2}=-\beta\frac{\partial\psi_\infty}{\partial x}, \tag{11}$$

which is essentially the vorticity equation considered in Rossby (1939). It can be verified that

$$\psi_\infty=-Uy-\frac{A}{k}\cos(kx-\omega t) \tag{12}$$

is a solution of (11) provided the frequency ω satisfies the Rossby dispersion relation,

$$\omega=kU-\frac{\beta}{k}. \tag{13}$$

The amplitude A and wavenumber k ($\equiv 2\pi/L$) are constants which, without loss of generality, are taken as positive, while ω is a constant that can be positive or negative; if $\omega<0$, the wave retrogresses. From (12) we obtain the remote wind components as

$$u_\infty=U, \quad v_\infty=A\sin(kx-\omega t). \tag{14}$$

In the steady-periodic state, u and v must satisfy the temporal periodicity condition

$$u|_{t=0}=u|_{t=\tau}, \quad v|_{t=0}=v|_{t=\tau}, \tag{15}$$

where $\tau\equiv 2\pi/|\omega|$ is the wave period.[1] Additionally, as the time of day must be the same at the start and end times of the wave passage (for the sake of definiteness, let the start time $t=0$ correspond to the first sunrise), the wave period must be an integral number N_τ of days,

$$\tau=N_\tau t_{24}, \tag{16}$$

where $t_{24}\equiv 24$ h. In view of $\tau\equiv 2\pi/|\omega|$, (16), and the fact that $\omega=|\omega|\,\mathrm{sgn}\omega$ ($\mathrm{sgn}\omega$ is the unit sign function; $\mathrm{sgn}\omega\equiv -1, 0, 1$ for $\omega<0$, $\omega=0$, $\omega>0$, respectively), we can write

$$\omega=\frac{\Omega}{N_\tau}\mathrm{sgn}\omega, \tag{17}$$

which shows that the diurnal frequency Ω is an integral multiple N_τ of the wave frequency.

Since the perturbation pressure gradient is independent of z, its components can be inferred from (8), (9), and (14) to be

$$\frac{\partial\Pi}{\partial x}=fv_\infty-\frac{\partial u_\infty}{\partial t}-U\frac{\partial u_\infty}{\partial x}=fv_\infty=fA\sin(kx-\omega t), \tag{18}$$

$$\frac{\partial\Pi}{\partial y}=-fu_\infty-\frac{\partial v_\infty}{\partial t}-U\frac{\partial v_\infty}{\partial x}=-fU+A(\omega-kU)\cos(kx-\omega t). \tag{19}$$

[1] Although the Rossby wave in our study has a single frequency, that frequency can be thought of, more broadly, as representing the dominant Fourier component in a continuous power density spectrum.

Integration of (18) produces $\Pi = -(fA/k)\cos(kx - \omega t) + \eta(y)$, where $\eta(y)$ is a function of integration. Substituting this expression into (19), and using $df/dy = \beta$ and $\omega - kU = -\beta/k$ [from (13)], yields $d\eta/dy = -fU$. This integrates to $\eta(y) = -U\int^y f\,dy' \approx -Ufy$, where an irrelevant constant of integration has been omitted [if retained, the constant would appear as an additive constant for Π (via η), vanish from $\partial\Pi/\partial x$ and $\partial\Pi/\partial y$, and not affect the wind field]. We obtain Π as

$$\Pi = -\frac{fA}{k}\cos(kx - \omega t) - Ufy, \tag{20}$$

or, in view of (12),

$$\Pi = f\psi_\infty. \tag{21}$$

Thus, isolines of Π drawn in the x–y plane coincide with streamlines for the remote flow (u_∞, v_∞). It can be noted that (21) is satisfied by geostrophic flows (Pedlosky 1987), but our remote flow is not exactly geostrophic. Equations (18) and (19) (evaluated with $\omega - kU = -\beta/k$) yield height-independent geostrophic wind components $u_g \equiv -(1/f)\partial\Pi/\partial y$ and $v_g \equiv (1/f)\partial\Pi/\partial x$ as

$$u_g = u_\infty + \frac{\beta A}{fk}\cos(kx - \omega t), \quad v_g = v_\infty. \tag{22}$$

Thus, v_∞ is geostrophically balanced, but u_∞ is not. However, for parameters typical of midlatitude Rossby waves, $\beta A/fk \ll u_\infty$, so u_∞ is nearly geostrophic [e.g., $A = 10$ m s^{-1}, $L = 5000$ km ($k \approx 1.26 \times 10^{-6}$ m^{-1}), and $\phi = 40°$N ($f \approx 9.35 \times 10^{-5}$ s^{-1}; $\beta \approx 1.77 \times 10^{-11}$ m^{-1} s^{-1}) yield $\beta A/fk \approx 1.5$ m s^{-1}, which is much less than a typical u_∞, which is on the order of 10 m s^{-1}].

c. *Complex wind deviation*

Applying (18) and (19) in (1) and (2) (and using $du_\infty/dz = dv_\infty/dz = 0$) yields

$$\frac{\partial}{\partial t}(u - u_\infty) + U\frac{\partial}{\partial x}(u - u_\infty) = f(v - v_\infty) + K(t)\frac{\partial^2}{\partial z^2}(u - u_\infty) - R(u - u_\infty), \tag{23}$$

$$\frac{\partial}{\partial t}(v - v_\infty) + U\frac{\partial}{\partial x}(v - v_\infty) = -f(u - u_\infty) + K(t)\frac{\partial^2}{\partial z^2}(v - v_\infty) - R(v - v_\infty). \tag{24}$$

Multiplying (24) by the imaginary unit i ($\equiv\sqrt{-1}$), and adding the result to (23) yields

$$\frac{\partial Q}{\partial t} + U\frac{\partial Q}{\partial x} = -(R + if)Q + K(t)\frac{\partial^2 Q}{\partial z^2}, \tag{25}$$

where

$$Q(x, z, t) \equiv (u - u_\infty) + i(v - v_\infty) \tag{26}$$

is the complex wind deviation (deviation of u and v from their remote values). In terms of Q, the no-slip condition (5) becomes

$$Q|_{z=0} = -(u_\infty + iv_\infty), \tag{27}$$

the lateral periodicity condition (7) becomes

$$Q|_{x=0} = Q|_{x=L}, \tag{28}$$

the remote condition (14) becomes

$$\lim_{z\to\infty} Q = 0, \tag{29}$$

and the temporal periodicity condition (15) becomes

$$Q|_{t=0} = Q|_{t=\tau}. \tag{30}$$

It is shown in appendix B that if a solution of (25) subject to (27)–(30) exists, it is unique.

Once Q is known, u and v follow from the real ($\Re$) and imaginary ($\Im$) parts of (26) as

$$u = u_\infty + \Re(Q), \qquad v = v_\infty + \Im(Q). \tag{31}$$

Integrating (3) upward from the ground, where (6) applies, then yields w as

$$w = -\Re\left[\frac{\partial}{\partial x}\int_0^z Q(x, z', t)dz'\right]. \tag{32}$$

3. Sidelight: Inviscid nocturnal flow calculation

Before solving the viscous problem of section 2, we consider the simpler problem where K vanishes at sunset, and remains zero through the night, as in the Blackadar (1957) model (although, unlike that model, our pressure gradient varies with x and t). The inviscid solutions for u, v, and the horizontal divergence of the wind field (divergence) are simple enough that they lead to explicit formulas for the locations and magnitudes of the extrema of those variables. The inviscid flow will be compared with the viscous flow during the night in section 7.

The inviscid ($K = 0$) undamped ($R = 0$) version of (25) is the first-order linear equation

$$\frac{\partial Q}{\partial t} + U\frac{\partial Q}{\partial x} = -ifQ. \tag{33}$$

Using the method of characteristics, we obtain the general solution of (33) for each night as

$$Q = \exp(-ift)H(x - Ut), \tag{34}$$

where $H(x - Ut)$ is an unknown function. It can be shown that $|H|$ is the deviation flow speed. We obtain $H(x - Ut)$ for each night by specifying the initial (sunset) winds at a low altitude ($z = z_{\text{low}}$) where NLLJs in real ABLs typically develop. Due to friction, these low-level winds are weaker than the corresponding remote winds. It is convenient to specify these

low-level winds as a fraction ϵ (wind fraction parameter, $0 < \epsilon < 1$) of the remote winds:

$$u|_{\substack{z=z_{\text{low}}\\ t=t_{N\text{set}}}} = \epsilon u_\infty|_{t=t_{N\text{set}}} = \epsilon U,$$
$$v|_{\substack{z=z_{\text{low}}\\ t=t_{N\text{set}}}} = \epsilon v_\infty|_{t=t_{N\text{set}}} = \epsilon A \sin(kx - \omega t_{N\text{set}}), \quad (35)$$

where $t_{N\text{set}}$ is the time of the $(N + 1)$th sunset ($N = 0, 1, \ldots, N_\tau - 1$). Using (13), (14), and (35) to evaluate (26) at $t = t_{N\text{set}}$ yields $Q|_{t=t_{N\text{set}}} = -(1 - \epsilon)[U + iA\sin(kx - \omega t_{N\text{set}})] = -(1 - \epsilon)\{U + iA\sin[k(x - Ut_{N\text{set}}) + \beta t_{N\text{set}}/k]\}$. Applying this result in (34) at $t = t_{N\text{set}}$ yields $H(x - Ut_{N\text{set}}) = -(1 - \epsilon) \times \exp(ift_{N\text{set}})\{U + iA\sin[k(x - Ut_{N\text{set}}) + \beta t_{N\text{set}}/k]\}$ from which we see that

$$H(x - Ut) = -(1 - \epsilon)\exp(ift_{N\text{set}})\{U + iA\sin[k(x - Ut) + \beta t_{N\text{set}}/k]\}. \quad (36)$$

Application of (36) in (34) yields

$$Q = -(1 - \epsilon)\exp[-if(t - t_{N\text{set}})]\{U + iA\sin[k(x - Ut) + \beta t_{N\text{set}}/k]\}, \quad (37)$$

and u and v follow from (31) as

$$u = U - (1 - \epsilon)U\cos[f(t - t_{N\text{set}})] - (1 - \epsilon)A\sin[f(t - t_{N\text{set}})] \times \sin[k(x - Ut) + \beta t_{N\text{set}}/k], \quad (38)$$

$$v = A\sin(kx - \omega t) - (1 - \epsilon)A\cos[f(t - t_{N\text{set}})]\sin[k(x - Ut) + \beta t_{N\text{set}}/k] + (1 - \epsilon)U\sin[f(t - t_{N\text{set}})]. \quad (39)$$

The divergence, $\delta \equiv \partial u/\partial x + \partial v/\partial y = \partial u/\partial x$, follows from (38) as

$$\delta = -(1 - \epsilon)Ak\sin[f(t - t_{N\text{set}})]\cos[k(x - Ut) + \beta t_{N\text{set}}/k]. \quad (40)$$

Thus, δ is proportional to Ak.

The local extrema of u are the zeros of δ, which, in view of (40) occur at the points $x = x_u(t)$ for which $k(x_u - Ut) + \beta t_{N\text{set}}/k = \pi/2 + n\pi$ (n is any integer), that is,

$$x_u = Ut - \frac{\beta t_{N\text{set}}}{k^2} + \frac{\pi}{k}\left(\frac{1}{2} + n\right). \quad (41)$$

Thus, the u extrema move with the westerly current. Equation (41) and analogous equations for the local extrema of v and δ sometimes place an extremum outside of the domain of interest ($0 \le x \le L$). Since the flow is periodic in x, it is legitimate to shift such a location an integral number of wavelengths to an equivalent location within the domain. Applying (41) in (38) yields the peak values $u_{\text{peak}}(t)$ of u as

$$u_{\text{peak}} = U - (1 - \epsilon)U\cos[f(t - t_{N\text{set}})] + (-1)^{n+1}(1 - \epsilon)A\sin[f(t - t_{N\text{set}})]. \quad (42)$$

Since n only appears in (42) through the factor $(-1)^{n+1}$, all $u_{\text{peak}}(t)$ profiles obtained with any even n are the same. Similarly, all $u_{\text{peak}}(t)$ profiles obtained with any odd n are the same. Thus, (42) yields two solutions for u_{peak} at any time. This should not be surprising since one wavelength of the Rossby wave is composed of one ridge and one trough.

Equation (40) also shows that the extrema of δ occur at the points $x = x_{\text{div}}(t)$ for which

$$x_{\text{div}} = Ut - \frac{\beta t_{N\text{set}}}{k^2} + \frac{l\pi}{k}, \quad (43)$$

where l is an integer. Thus, the extrema of δ also move with the westerly current. The peak values $\delta_{\text{peak}}(t)$ of δ follow from (43) and (40) as

$$\delta_{\text{peak}} = (-1)^{l+1}(1 - \epsilon)Ak\sin[f(t - t_{N\text{set}})]. \quad (44)$$

There are two δ extrema, one associated with any even l, and the other with any odd l. Since w can be expressed as a vertical integral of δ, its extrema also move with the westerly current and have magnitudes that are proportional to Ak.

As shown in appendix C, the extrema of v occur at the points $x = x_v(t)$ for which

$$x_v = Ut - \frac{\mu(t)}{k} + \frac{\pi}{k}\left(\frac{1}{2} + q\right), \quad (45)$$

where $\mu(t)$ is obtained from (C4) or (C5) (see discussion following those equations), and q is an integer. The two peak values v_{peak} of v are given by

$$v_{\text{peak}} = U\sin[f(t - t_{N\text{set}})] + (-1)^q A\Gamma(t), \quad (46)$$

where q is an integer (any even q yields one extremum, and any odd q yields the other), and

$$\Gamma \equiv \sqrt{1 + (1 - \epsilon)^2\cos^2[f(t - t_{N\text{set}})] - 2(1 - \epsilon)\cos[f(t - t_{N\text{set}})]\cos[\beta(t - t_{N\text{set}})/k]}. \quad (47)$$

As the radicand in (47) can be shown to be positive, $\Gamma(t)$ is real and positive.

4. Viscous solution

The viscous problem of section 2 is derived for the general case where the eddy viscosity is a diurnally varying but otherwise arbitrary function of time. Motivated by the forms of (14), (27), and (28), we consider the trial solution

$$Q = P_0 + P_1\exp(ikx) + P_{-1}\exp(-ikx), \quad (48)$$

where $P_j = P_j(z, t)$ ($j = -1, 0, 1$). Applying (48) in (27), with $\sin(kx - \omega t)$ in v_∞ expanded out as $[\exp(ikx)\exp(-i\omega t) - \exp(-ikx)\exp(i\omega t)]/(2i)$ produces $P_{-1}(0, t) = (A/2)\exp(i\omega t)$,

$P_0(0, t) = -U$, and $P_1(0, t) = -(A/2)\exp(-i\omega t)$ or, more succinctly,

$$P_j(0, t) = [(j^2 - 1)U - jA/2]\exp(-ij\omega t), \quad j = -1, 0, 1. \quad (49)$$

Substituting (48) into (29), (30), and (25) yields

$$\lim_{z\to\infty} P_j(z, t) = 0, \quad j = -1, 0, 1, \quad (50)$$

$$P_j(z, 0) = P_j(z, \tau), \quad j = -1, 0, 1, \quad (51)$$

$$\frac{\partial P_j}{\partial t} = -[R + i(f + jkU)]P_j + K(t)\frac{\partial^2 P_j}{\partial z^2}, \quad j = -1, 0, 1. \quad (52)$$

Equations similar to (52) appear in one-dimensional studies of NLLJs and temporally varying Ekman layers, though usually in the context of an initial value problem or, if a steady-periodic solution is sought, single-frequency oscillations of the eddy viscosity. A notable exception is the Ooyama (1957) theory for wind oscillations due to diurnal variations of the eddy viscosity when the pressure gradient force is constant in space and time. Our solution framework is similar to that of Ooyama (1957), despite the spatial and temporal variations in our pressure gradient force. Applying P_j in the separated variables form,

$$P_j = Z_j(z)T_j(t) \quad (53)$$

in (52) yields

$$\frac{1}{T_j}\frac{dT_j}{dt} = -[R + i(f + jkU)] + \frac{K(t)}{Z_j}\frac{d^2 Z_j}{dz^2}, \quad (54)$$

from which follow

$$\frac{dT_j}{dt} = -[R + i(f + jkU) + \lambda_j K(t)]T_j, \quad (55)$$

$$\frac{d^2 Z_j}{dz^2} + \lambda_j Z_j = 0, \quad (56)$$

where the λ_j are separation constants. The general solutions of (55) and (56) are

$$T_j = C_j \exp\left\{-[R + i(f + jkU)]t - \lambda_j\int_0^t K(t')dt'\right\}, \quad (57)$$

$$Z_j = A_j \exp(iz\sqrt{\lambda_j}) + B_j \exp(-iz\sqrt{\lambda_j}), \quad (58)$$

where A_j, B_j, and C_j are constants. In view of (53), (50), and (58), either $A_j = 0$ or $B_j = 0$, and we can write P_j as

$$P_j = D_j \exp\left\{\pm iz\sqrt{\lambda_j} - [R + i(f + jkU)]t - \lambda_j\int_0^t K(t')dt'\right\}, \quad (59)$$

where D_j are constants. The $\pm$ symbol in (59) is shorthand for whatever sign gives $\pm i\sqrt{\lambda_j}$ a negative real part. Applying (59) in the periodicity condition (51) yields

$$1 = \exp\{-\tau[R + \lambda_j\overline{K} + i(f + jkU)]\}, \quad (60)$$

where

$$\overline{K} \equiv \frac{1}{\tau}\int_0^\tau K(t')dt'. \quad (61)$$

Taking ln of (60), with 1 written as $\exp(2m\pi i)$ (m is an integer), yields a λ_j for each m as

$$\lambda_{jm} = -\frac{R + i(f + jkU + 2m\pi/\tau)}{\overline{K}}. \quad (62)$$

Generalized to include all λ_{jm}, (59) appears as

$$P_j = \exp\{-[R + i(f + jkU)][t - \kappa(t)]\}\sum_{m=-\infty}^{\infty} D_{jm}F_m(t) \times \exp(\pm iz\sqrt{\lambda_{jm}}), \quad (63)$$

where

$$F_m(t) \equiv \exp[2m\pi i\kappa(t)/\tau], \quad (64)$$

$$\kappa(t) \equiv \frac{1}{\overline{K}}\int_0^t K(t')dt', \quad (65)$$

and the D_{jm} are constants.

From (64) it can be seen that the $F_m(t)$ are periodic with a fundamental period of τ. Apart from a minor difference (arbitrary τ in place of 24-h period τ_{24}), these $F_m(t)$ satisfy the same orthogonality relation derived in Shapiro et al. (2016), namely

$$\int_0^\tau K(t')F_m(t')F_n^*(t')dt' = \delta_{mn}\tau\overline{K}, \quad (66)$$

where δ_{mn} is the Kronecker delta, and an asterisk (*) denotes complex conjugation.

It is convenient to put the λ_{jm} in the polar form

$$\lambda_{jm} = -r_{jm}\exp(i\theta_{jm}), \quad (67)$$

where

$$r_{jm} \equiv \frac{\sqrt{R^2 + (f + jkU + 2m\pi/\tau)^2}}{\overline{K}}, \quad (68)$$

$$\theta_{jm} \equiv \tan^{-1}\left(\frac{f + jkU + 2m\pi/\tau}{R}\right), \quad (69)$$

and the inverse tangent $\tan^{-1}$ is defined by its principal value (so $-\pi/2 \le \theta_{jm} \le \pi/2$). In view of (67)–(69), we can write (63) as

$$P_j = \exp\{-[R + i(f + jkU)][t - \kappa(t)]\}\sum_{m=-\infty}^{\infty} D_{jm}F_m(t) \times \exp[-zr_{jm}^{1/2}\exp(i\theta_{jm}/2)], \quad (70)$$

where the fact that $-\pi/4 \le \theta_{jm}/2 \le \pi/4$ [so $\cos(\theta_{jm}/2) \ge 0$] has informed the sign choice for the $\pm$ symbol. To get D_{jm}, set $z = 0$ in (70) and use (49) for $P_j(0, t)$, obtaining

$$\sum_{m=-\infty}^{\infty} D_{jm}F_m(t) = [(j^2 - 1)U - jA/2]\exp\{[R + i(f + jkU)] \times [t - \kappa(t)] - ij\omega t\}. \quad (71)$$

Multiplying (71) by $K(t)F_p^*(t)$ (p is an integer), integrating the resulting equation over one period [using (66)], and renaming the dummy index ($p \to m$) then yields D_{jm} as

$$D_{jm} = E_j\int_0^\tau K(t')F_m^*(t')\exp\{[R + i(f + jkU)][t' - \kappa(t')] - ij\omega t'\}dt', \quad (72)$$

where

$$E_j \equiv \frac{(j^2 - 1)U - jA/2}{\tau\overline{K}}. \quad (73)$$

With Q thus determined, u and v readily follow from (31). We obtain w from (32) as

$$w = \Re\left[ik\exp(-ikx)\int_0^z P_{-1}(z', t)dz' - ik\exp(ikx)\int_0^z P_1(z', t)dz'\right], \quad (74)$$

where the integrals are evaluated as

$$\int_0^z P_j(z', t)dz' = -\exp\{-[R + i(f + jkU)][t - \kappa(t)]\} \times \sum_{m=-\infty}^{\infty} D_{jm}\exp(-i\theta_{jm}/2)F_m(t)\left\{\frac{\exp[-zr_{jm}^{1/2}\exp(i\theta_{jm}/2)] - 1}{r_{jm}^{1/2}}\right\}, \quad [j = -1, 1]. \quad (75)$$

The integral of P_0 does not appear in (74) since the part of u associated with $j = 0$ is horizontally uniform (horizontally nondivergent). It can be inferred from (68), (69), and (72)–(75) that

$$w \propto kA, \quad (76)$$

as in the inviscid theory, provided the Rossby number kU/f is much less than 1.

The solution procedure can be summarized as:

Step 1. Specify the governing parameters and the explicit form of $K(t)$.
Step 2. Get $\overline{K}$ from (61).
Step 3. Get $\kappa(t)$ from (65), r_{jm} from (68), and θ_{jm} from (69).
Step 4. Get $F_m(t)$ from (64).
Step 5. Get D_{jm} from (72).
Step 6. Get P_j from (70).
Step 7. Get Q from (48).
Step 8. Get u and v from (31), and w from (74).

5. Solution breakdown/resonance and critical latitudes

If there is no Rayleigh damping ($R = 0$), (68) reduces to $r_{jm} = |f + jkU + 2m\pi/\tau|/\overline{K}$, which vanishes for

$$f + jkU + 2m\pi/\tau = 0. \quad (77)$$

Here, f is the inertial frequency, kU is the advection frequency, and $2m\pi/\tau$ is a harmonic of the Rossby wave frequency [of which the diurnal frequency is an integral multiple; see (17)]. When $r_{jm} = 0$, the z-dependent exponential in (70) is 1 for all z, which violates (50). Additionally, the term enclosed by curly brackets in the sum in (75) is indeterminate. Application of L'Hôpital's rule as $r_{jm} \to 0$ shows that this term is proportional to z and therefore blows up as $z \to \infty$. Since the $j = \pm 1$ integrals in (75) appear in (74), w blows up as $z \to \infty$. However, there are no obvious implications of the $r_{jm} = 0$ condition for the magnitudes of u or v.

Using (13), (16), and (17), we can rewrite (77) as $f + (j + m\,\mathrm{sgn}\omega)\Omega/N_\tau + j\beta/k = 0$ or, since $f = 2\Omega\sin\phi$ and $\beta = (2\Omega/a)\cos\phi$,

$$\sin\phi + \frac{j}{ak}\cos\phi = -\frac{j + m\,\mathrm{sgn}\omega}{2N_\tau}. \quad (78)$$

Thus, the solution breaks down for $R = 0$ at latitudes satisfying (78). However, if $R \ne 0$ then $r_{jm} \ne 0$, and the z-dependent exponential in (70) and term enclosed by curly brackets in (75) are well behaved.

We are interested in the magnitude of w and the extent to which the wind deviations extend upward when (77) [equivalently (78)] is satisfied, even when breakdown cannot occur ($R \ne 0$). In view of (70), (74), and (75), the m having the greatest impact are those associated with the largest D_{jm}. We apply (64) in (72), and arrange the result so that the imaginary terms in the exponential are grouped into terms that are proportional to t' and terms that are proportional to $\kappa(t')$, namely

$$D_{jm} = E_j\int_0^\tau K(t')\exp\{R[t' - \kappa(t')] + i(f + jkU - j\omega)t' - i(f + jkU + 2m\pi/\tau)\kappa(t')\}dt'. \quad (79)$$

Applying (77) in (79) to eliminate $f + jkU$, followed by use of $\tau = 2\pi/|\omega|$ and (17), yields

$$D_{jm} = E_j\int_0^\tau K(t')\exp\{R[t' - \kappa(t')] - i(m + j\,\mathrm{sgn}\omega)(\Omega/N_\tau)t'\}dt'. \quad (80)$$

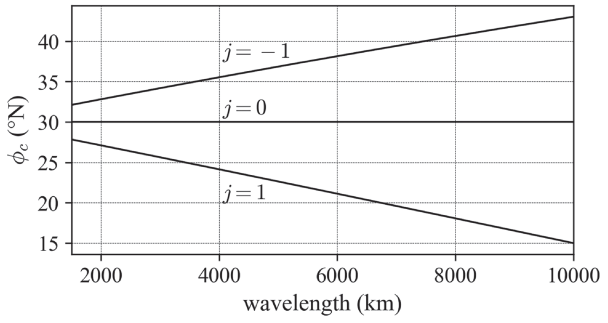

FIG. 1. Critical latitudes ϕ_c vs wavelength in the Northern Hemisphere predicted from (83). There are three critical latitudes for u and v (corresponding to $j = -1, 0$, and 1) but only two critical latitudes for w (corresponding to $j = -1$ and $j = 1$).

We anticipate that this integral is maximized when the oscillation frequency of the exponential [which is $(m + j\,\mathrm{sgn}\omega)\Omega/N_\tau$] matches that of K (which is Ω). This occurs for

$$m + j\,\mathrm{sgn}\omega = \pm N_\tau. \tag{81}$$

Since j, $\mathrm{sgn}\omega$, and N_τ are integers, there is always an m for which (81) is satisfied. Multiplying (81) by $\mathrm{sgn}\omega$, and applying the resulting expression in (78) yields

$$\sin\phi + \frac{j}{ak}\cos\phi = \mp\frac{1}{2}\,\mathrm{sgn}\omega. \tag{82}$$

For typical midlatitude Rossby waves, $\beta/k < \Omega$, and use of the definitions of β and f shows that $|j(ak)^{-1}\cos\phi| < |\sin\phi|$. Accordingly, the $\mp$ symbol in (82) is $+\mathrm{sgn}\omega$ in the Northern Hemisphere and $-\mathrm{sgn}\omega$ in the Southern Hemisphere. Restricting attention to the Northern Hemisphere, we write (82) as $\sqrt{1+j^2/(ak)^2}\,\sin(\phi+\gamma) = 1/2$, where $\sin\gamma = j/[ak\sqrt{1+j^2/(ak)^2}]$ and $\cos\gamma = 1/\sqrt{1+j^2/(ak)^2} > 0$. The solution (with ϕ labeled as the critical latitude ϕ_c) then follows as

$$\phi_c = \sin^{-1}\left[\frac{1/2}{\sqrt{1+j^2/(ak)^2}}\right] - \sin^{-1}\left[\frac{j/(ak)}{\sqrt{1+j/(ak)^2}}\right], \quad [f > 0]. \tag{83}$$

For $j = 0$ (which affects u and v, but not w), (83) yields $\phi_c = 30°\mathrm{N}$, the critical latitude identified in the NLLJ and upper-ocean Ekman layer studies discussed in the introduction. For $j = 1$ and $j = -1$ (which affect u, v, and w), ϕ_c depends on the nondimensional wavenumber ak. These critical latitudes are graphed in Fig. 1.

6. Solution for $K(t)$ with piecewise constant diurnal variations

In this section we adapt the general viscous solution of section 4 to the case where K is a piecewise constant function of time that increases abruptly at sunrise from a small nighttime value K_n to a large daytime value K_d, and decreases abruptly at sunset back to K_n. We work with the day number function $N(t) \equiv \mathrm{int}(t/t_{24})$, which generates the sequence of 24-h intervals (days) $Nt_{24} \le t < (N+1)t_{24}$ for $N = 0, 1, \ldots, N_\tau - 1$. Corresponding to $N = 0$ is the first day, $0 \le t < t_{24}$, and to $N = N_\tau - 1$ is the last day, $(N_\tau - 1)t_{24} \le t < N_\tau t_{24}$. Thus, $t = Nt_{24}$ corresponds to sunrise at the start of the $(N+1)$th day. With t_{set} denoting the first ($N = 0$) sunset, and $t_{N\mathrm{set}} \equiv Nt_{24} + t_{\mathrm{set}}$ denoting sunset on the $(N+1)$th day, we can write $K(t)$ as

$$K(t) = \begin{cases} K_d, & t \in \mathrm{DAY}, \\ K_n, & t \in \mathrm{NIGHT}, \end{cases} \tag{84}$$

where the daytime (DAY) and nighttime (NIGHT) intervals are

$$\mathrm{DAY} \equiv \bigcup_{N=0}^{N_\tau-1} \{t | Nt_{24} \le t < Nt_{24} + t_{\mathrm{set}}\}, \tag{85}$$

$$\mathrm{NIGHT} \equiv \bigcup_{N=0}^{N_\tau-1} \{t | Nt_{24} + t_{\mathrm{set}} \le t < (N+1)t_{24}\}. \tag{86}$$

In view of (84)–(86), (61) becomes

$$\overline{K} = K_d\frac{t_{\mathrm{set}}}{t_{24}} + K_n\left(1 - \frac{t_{\mathrm{set}}}{t_{24}}\right), \tag{87}$$

(65) becomes,

$$\kappa(t) = \begin{cases} Nt_{24} + K_d(t - Nt_{24})/\overline{K}, & t \in \mathrm{DAY}, \\ Nt_{24} + [K_d t_{\mathrm{set}} + K_n(t - Nt_{24} - t_{\mathrm{set}})]/\overline{K}, & t \in \mathrm{NIGHT}, \end{cases} \tag{88}$$

and (72) becomes

$$D_{jm} = E_j \sum_{N=0}^{N_\tau-1} \left\{ K_d \int_{Nt_{24}}^{Nt_{24}+t_{\mathrm{set}}} \exp[\Phi_{jm}(t')]dt' + K_n \int_{Nt_{24}+t_{\mathrm{set}}}^{(N+1)t_{24}} \exp[\Phi_{jm}(t')]dt' \right\}, \tag{89}$$

where

$$\Phi_{jm}(t) \equiv \{R + i[f + j(kU - \omega)]\}t - [R + i(f + jkU + 2m\pi/\tau)]\kappa(t). \tag{90}$$

Applying (88) in (90) yields Φ_{jm} as the piecewise linear-in-t form,

$$\Phi_{jm}(t) = \begin{cases} c_{jm}t + b_{jm}N(t_{24} - t_{\mathrm{set}}), & t \in \mathrm{DAY}, \\ d_{jm}t - b_{jm}(N+1)t_{\mathrm{set}}, & t \in \mathrm{NIGHT}, \end{cases} \tag{91}$$

$$b_{jm} \equiv -\lambda_{jm}(K_d - K_n), \tag{92}$$

TABLE 1. Input parameters for experiments L2000 and L6000. These are also the default values for further experiments in which one parameter is varied at a time.

Expt	L (km)	N_τ	sgnω	ϕ (°N)	A (m s^{-1})	$t_{\rm set}$ (h)	K_d (m^2 s^{-1})	K_n (m^2 s^{-1})	R^{-1} (days)
L2000	2000	3	+1	40	20	14	50	2	5
L6000	6000	7	−1	40	20	14	50	2	5

$$c_{jm} \equiv -\lambda_{jm}(\overline{K} - K_d) - i(\omega j + 2m\pi/\tau), \tag{93}$$

$$d_{jm} \equiv -\lambda_{jm}(\overline{K} - K_n) - i(\omega j + 2m\pi/\tau), \tag{94}$$

where λ_{jm} was defined in (62). Evaluating the integrals in (89) using (91)–(94) and the derived relation $b_{jm} + c_{jm} = d_{jm}$, noting that the integrals multiplying K_d involve $t \in$ DAY, while the integrals multiplying K_n involve $t \in$ NIGHT, yields

$$D_{jm} = E_j\left[\frac{K_n}{d_{jm}}\exp(p_{jm}) + \left(\frac{K_d}{c_{jm}} - \frac{K_n}{d_{jm}}\right)\exp(c_{jm}t_{\rm set}) - \frac{K_d}{c_{jm}}\right] \times \sum_{N=0}^{N_\tau-1}\exp(Np_{jm}), \tag{95}$$

where

$$p_{jm} \equiv d_{jm}t_{24} - b_{jm}t_{\rm set}. \tag{96}$$

The sum in (95) is evaluated for $p_{jm} \neq 0$ as

$$\sum_{N=0}^{N_\tau-1}\exp(Np_{jm}) = \sum_{N=0}^{N_\tau-1}[\exp(p_{jm})]^N = \frac{1-[\exp(p_{jm})]^{N_\tau}}{1-\exp(p_{jm})} = \frac{1-\exp(N_\tau p_{jm})}{1-\exp(p_{jm})}, \quad [p_{jm} \neq 0], \tag{97}$$

where we have used the formula for the sum of a finite geometric sequence. For $p_{jm} = 0$, the sum is evaluated directly as $\sum_{N=0}^{N_\tau-1} 1 = N_\tau$. It can be inferred from (92), (94), and (87) that $p_{jm} = 0$ for (i) $m = j$ if $\omega < 0$, (ii) $m = -j$ if $\omega > 0$, and (iii) all j and m if $\omega = 0$.

TABLE 2. Westerly current speed U vs the latitude ϕ obtained from (13) using the parameters in Table 1. U_{L2000} and U_{L6000} are the values of U from experiments in which $L = 2000$ km and $L = 6000$ km, respectively.

ϕ (°N)	$U_{\rm L2000}$ (m s^{-1})	$U_{\rm L6000}$ (m s^{-1})
20	9.89	9.64
30	9.72	8.11
40	9.49	6.03
50	9.20	3.46

7. Examples

We present examples of the piecewise-constant $K(t)$ flows considered in section 6. There are two main experiments: (i) L2000, for an eastward-propagating wave of relatively short wavelength ($L = 2000$ km), and (ii) L6000, for a westward-propagating wave of moderate wavelength ($L = 6000$ km). In both experiments, we take $\phi = 40°$N ($f \approx 9.35 \times 10^{-5}$ s^{-1}), $A = 20$ m s^{-1}, $t_{\rm set} = 14$ h, $K_d = 50$ m^2 s^{-1}, $K_n = 2$ m^2 s^{-1}, and $R = (5\ {\rm days})^{-1}$. The value of R is consistent with guidance from D'Asaro (1985) that $R^2 \ll f^2$. The values for K_d and K_n were informed by estimates of K from laboratory experiments and atmospheric observations in statically unstable (relevant to daytime) conditions (Yamada and Mellor 1975; Tombrou et al. 2007; Dandou et al. 2009) and statically stable (relevant to nighttime) conditions (Sharan and Gopalakrishnan 1997; Mahrt and Vickers 2006; Dandou et al. 2009), and are similar to the values used in the NLLJ studies of Shapiro et al. (2016) and Shapiro et al. (2022). In L2000, the wave period is set at 3 days ($N_\tau = 3$) and sgn$\omega = 1$ [magnitude but not sign of ω is fixed by choice of N_τ; see (17)]. In L6000, we set $N_\tau = 7$ and sgn$\omega = -1$ (wave retrogresses).[2] The input parameters for these experiments are summarized in Table 1. These are also the default input parameters for L2000- and L6000-like experiments in which one parameter is varied at a time. In all experiments, the solutions are evaluated with a vertical grid spacing of $\Delta z = 25$ m, a horizontal grid spacing of $\Delta x = L/50$, a time step of $\Delta t = 180$ s, and m-summations truncated at $m = \pm 20\,000$. The solutions will be compared with the inviscid solutions from section 3 with $\epsilon = 0.5$, the optimal value as determined by trial and error. Note that we do not have the freedom to specify U as an independent parameter, but obtain it from the dispersion relation (13) as a residual. The derived values of U given in Table 2 show that U is relatively insensitive to latitude for $L = 2000$ km, but decreases with latitude for $L = 6000$ km. The Π field at $t = 0$ in these experiments is shown in Fig. 2. At this time, troughs are found along the edges of the domain ($x = 0$ and $x = L$), and a ridge is found along the center of the domain ($x = L/2$).

Hovmöller plots of Π, u, v, and w from experiment L2000 are shown in Fig. 3; u and v are shown at the heights of their maxima ($z_{u\max} \approx 375$ m, $z_{v\max} \approx 475$ m), w is shown at $z = 1000$ m, which is within or near the top of typical ABLs, and the Π panel is valid at all heights (recall that Π is

[2] As preliminary experiments using $N_\tau = 7$ but sgn$\omega = 1$ (westerly propagating wave) yielded values of U that were unrealistically large, we have restricted attention to the retrogressing case.

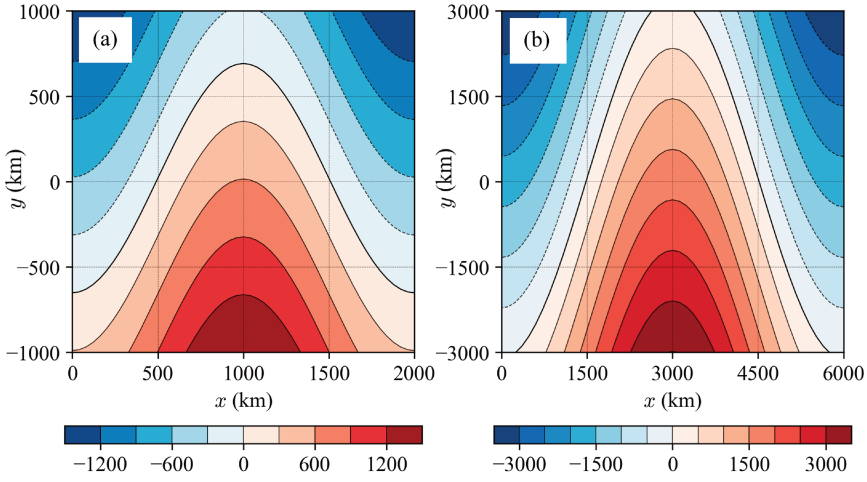

FIG. 2. Horizontal contour plots of Π ($m^2\ s^{-2}$) at $t = 0$ in experiments (a) L2000 and (b) L6000. In view of (21), isolines of Π drawn in the x–y plane coincide with remote ($z \to \infty$) flow streamlines.

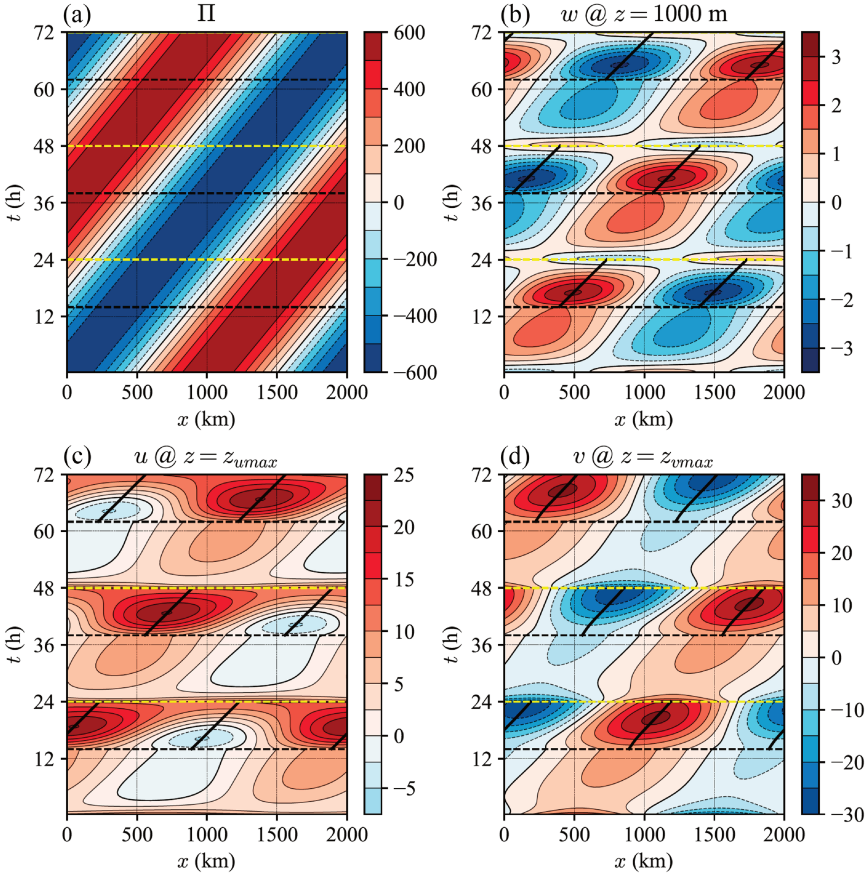

FIG. 3. Hovmöller plots from experiment L2000: (a) Π ($m^2\ s^{-2}$), (b) w (cm s^{-1}) at z = 1000 m, (c) u (m s^{-1}) at height of its maximum ($z_{u\max}$), and (d) v (m s^{-1}) at height of its maximum ($z_{v\max}$); $z_{u\max} \approx 375$ m, and $z_{v\max} \approx 475$ m. Thick dashed yellow and black lines indicate times of sunrise and sunset, respectively. Thick solid black curves track the locations of extrema (with respect to x) predicted by the inviscid theory for the nighttime intervals.

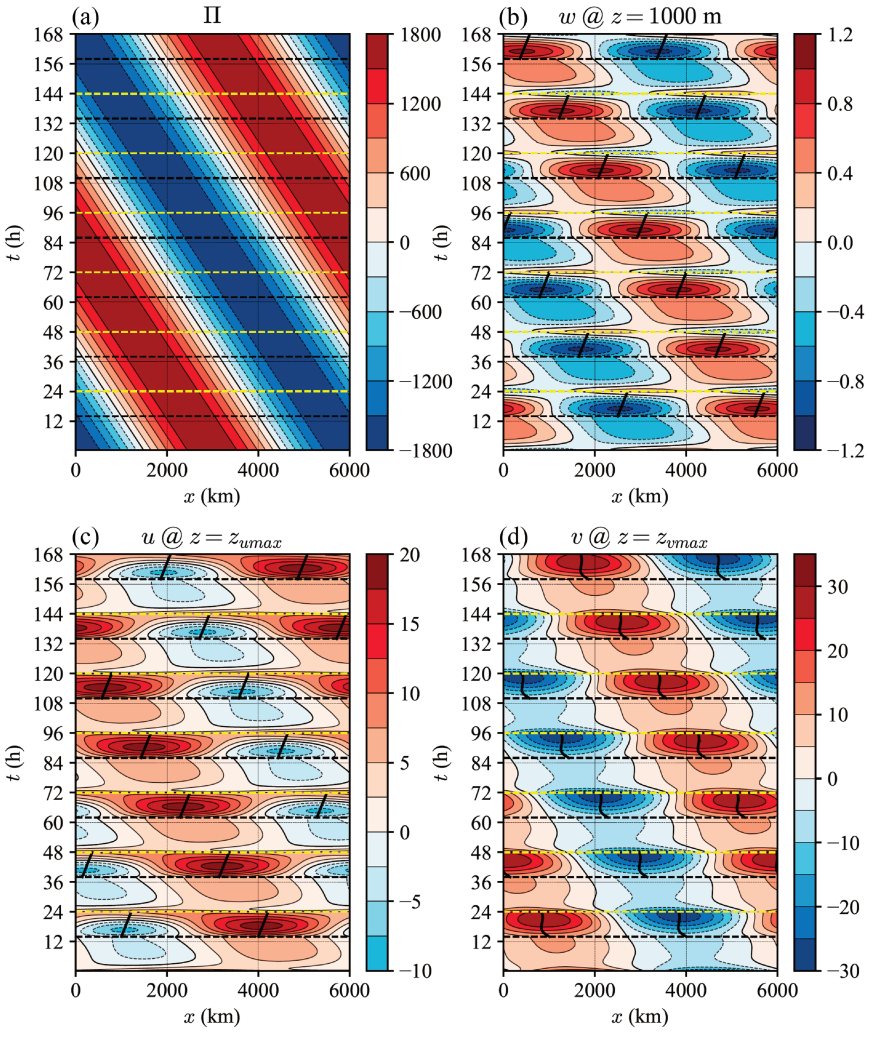

FIG. 4. As in Fig. 3, but for experiment L6000. Here, $z_{u\max} \approx 350$ m, and $z_{v\max} \approx 500$ m. Note that color bar bin intervals are different from those in Fig. 3.

independent of z). All fields except Π exhibit marked diurnal variations. There is a postsunset surge of alternating (with respect to x) convergent and divergent flow. The magnitudes and gradients of u, v, and w are weaker during the day than during the night (although this feature does not hold for w at higher levels; the height dependence of w will be discussed later). Consistent with the presence of a westerly current, the positive (westerly) peak value of u is larger than the magnitude of its largest negative (easterly) value of u. The peak westerly and easterly winds are found in the regions of strongest westerly- and easterly-directed pressure gradient forces, respectively. From the locations of the u-extrema we infer that the peak horizontal convergence ($-\partial u/\partial x$) is largest along the trough, where w attains its maximum. From the locations of the v-extrema we infer that the peak vertical vorticity ($\partial v/\partial x$) is also found along the trough. This finding is consistent with the formula for Ekman pumping [e.g., (4.5.39) of Pedlosky (1987)] in which w is directly proportional to the vertical vorticity.

Figure 3 also shows that NLLJ winds begin to develop shortly after sunset and reach peak intensity a few hours before sunrise. These winds undergo an anticyclonic rotation through the night (e.g., during the first night, the winds near the center of the domain veer from southeasterly shortly after sunset to southwesterly by sunrise). While such NLLJs are consistent with the inviscid Blackadar IO mechanism, they cannot be pure IOs since the pressure gradient force is time dependent. However, the u and v fields are in good agreement with the u and v predicted by our inviscid theory. For example, the locations of the extrema of u, v, and w are close to the locations $x_u(t)$, $x_v(t)$, and $x_{\text{div}}(t)$ given in (41), (45), and (43), respectively (solid black curves in Fig. 3). Additionally, the peak nighttime values of the inviscid solutions (42) for u_{peak} ($\approx$23.3 m s^{-1}) and (46) for v_{peak} ($\approx$31.0 m s^{-1}) closely match the peak values from

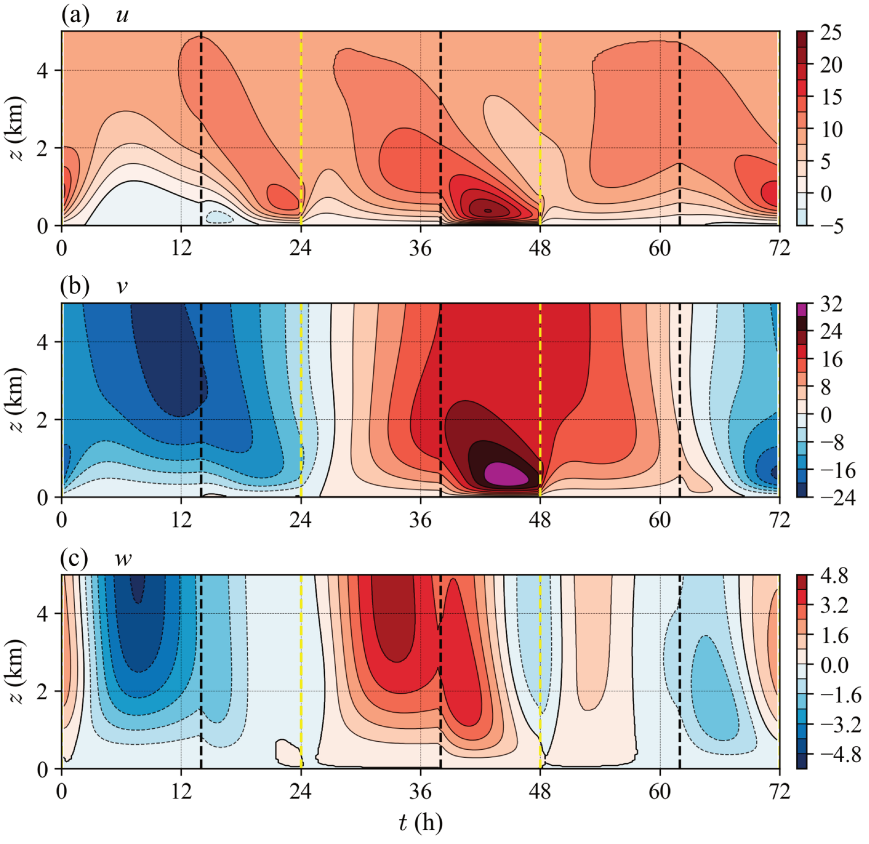

FIG. 5. Time–height plots of (a) u (m s^{-1}), (b) v (m s^{-1}), and (c) w (cm s^{-1}) at the x locations of their respective domain-wide maxima (though only the x location of nighttime maximum is considered for w) in experiment L2000. Thick dashed yellow and black lines indicate times of sunrise and sunset, respectively.

the model ($u_{max} \approx 22.6$ m s^{-1}, $v_{max} \approx 31.2$ m s^{-1}). The wind and vertical velocity fields weaken rapidly after sunrise.

The Hovmöller plots from experiment L6000 (Fig. 4) display many of the features seen in Fig. 3 for L2000, including a postsunset surge of convergent/divergent flow, the development of strong NLLJs with anticyclonically turning winds, and the rapid decay of u, v, and w after sunrise (presumably the changes to u, v, and w after sunrise and sunset would not have been as rapid if K had been specified to change gradually during the transition periods). The v_{max} in L6000 (≈30.0 m s^{-1}) is close to its value in L2000 (≈31.2 m s^{-1}). The somewhat larger difference between the u_{max} in L6000 (≈19.0 m s^{-1}) and L2000 (≈22.6 m s^{-1}) is consistent with the U obtained from the dispersion relation at 40°N being about 3.5 m s^{-1} larger in L2000 than in L6000 (Table 2). Again, our inviscid theory is in good agreement with the viscous model during the nighttime hours; the tracks of the peaks in the model-predicted u, v, and w are well represented by the inviscid curves, and the peak values from the inviscid solutions (42) and (46) ($u_{peak} \approx 17.7$ m s^{-1}, $v_{peak} \approx 29.6$ m s^{-1}) are close to the above-noted values for u_{max} and v_{max}.

Vertical cross sections of u, v, and w through the x locations of their maxima (though for w only the location of the nocturnal maximum is considered) are shown for L2000 in Fig. 5 and for L6000 in Fig. 6. Vertical cross sections of w through their daytime maxima (not shown) are fairly similar to these latter plots of w. The v panels show the development of NLLJs with peak v more than 50% greater than the peak remote value ($A = 20$ m s^{-1}). The peak jet winds in these experiments are found at $z = 600$ m (in L2000) and $z = 625$ m (in L6000). These heights are consistent with values documented in climatological studies; NLLJ winds typically peak at heights less than 1 km, and frequently at levels of 500 m or less (e.g., Whiteman et al. 1997; Song et al. 2005; Baas et al. 2009; Carroll et al. 2019). The w panels show two modes of ascent, an elevated mode that peaks in mid/late-afternoon and a lower-level mode that peaks a few hours after sunset. Although the afternoon peak is stronger than the nocturnal peak, the nocturnal peak is stronger than the daytime peak for $z < 2000$ m (recall the postsunset surge of w seen in Figs. 3b and 4b at $z = 1000$ m).

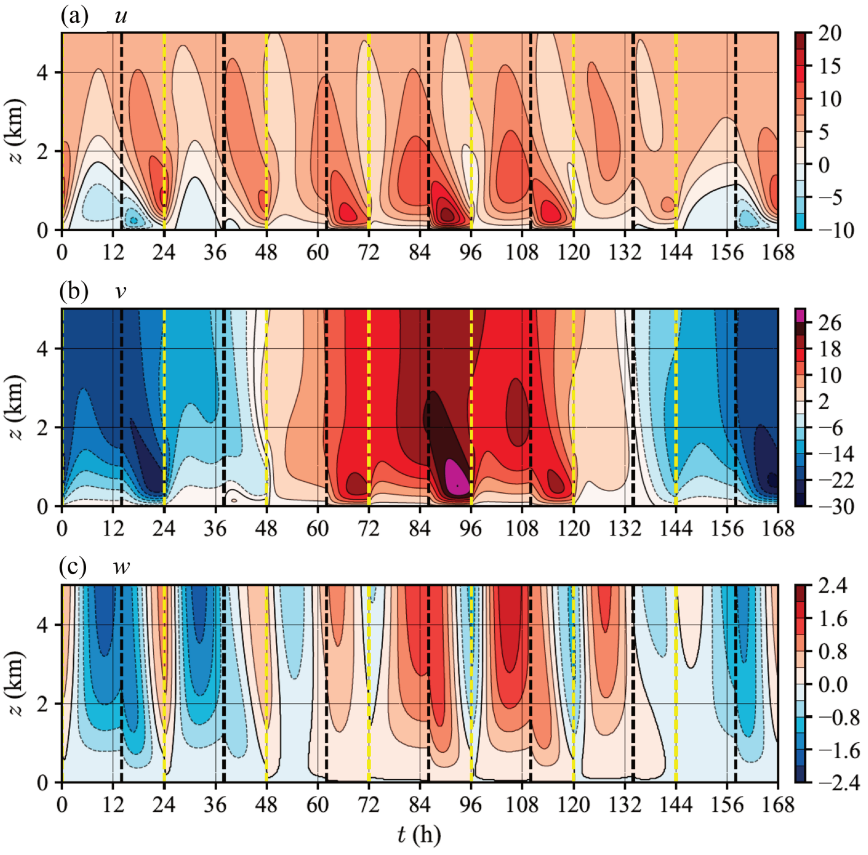

FIG. 6. As in Fig. 5, but for experiment L6000. Note that color bar bin intervals are different from those in Fig. 5.

Time series of the domain-maximum values u_{max}, v_{max}, and w_{max} from L2000 and L6000 are shown in Figs. 7 and 8 respectively.[3] Although none of u, v, or w is diurnally periodic (see Figs. 3–6), Figs. 7 and 8 show that u_{max}, v_{max}, and w_{max} are diurnally periodic. Not surprisingly, the peak remote values of u (i.e., the U given in Table 2 for 40°N: $U \approx 9.5$ m s^{-1} in L2000 and $U \approx 6.0$ m s^{-1} in L6000) and of v ($A = 20$ m s^{-1}) serve as floors for u_{max} and v_{max} over the wave period. The u_{max} and v_{max} panels show the NLLJ developing after sunset and decaying shortly after sunrise. The w_{max} panels show the main double-mode of ascent along with a weak third peak that arises when the late-night trend for w to increase is reversed by the sudden weakening of the convergent flow at sunrise. The overall peak w_{max} for $L = 2000$ km ($\approx$5.3 cm s^{-1}) is $\approx$2.5 times greater than that for $L = 6000$ km ($\approx$2.1 cm s^{-1}). This dependence of ascent on wavelength is slightly weaker than the factor of 3 increase implied by (76). The discrepancy may be due to the fact that the condition for the validity of (76) ($kU/f \ll 1$) is only marginally satisfied for $L = 2000$ km (kU/f is $\approx$0.067 for $L = 6000$ km but $\approx$0.318 for $L = 2000$ km).

Figures 7 and 8 also display time series from experiments in which K has no diurnal variations. We consider $K = 50$ m^2 s^{-1} (former daytime-only value) in one experiment, and $K = 2$ m^2 s^{-1} (former nighttime-only value) in another. Although the u and v in these constant-K experiments are temporally periodic with frequency ω (figures not shown), Figs. 7 and 8 show that u_{max} and v_{max} are temporally constant. Notably, for both L2000- and L6000-like experiments, the u_{max} and v_{max} obtained with $K = 50$ m^2 s^{-1} are the same as those obtained with $K = 2$ m^2 s^{-1}. The K-independence of these maxima is a feature of the classical Ekman solution [can be inferred from (4.3.21a) and (4.3.21b) of Pedlosky (1987)]. Additionally, consistent with the Ekman prediction that the heights of the wind maxima are proportional to the Ekman depth $(2K/f)^{1/2}$, the ratio of the heights of the peak u for the two constant-K L6000-like runs (1125 m/225 m = 5.0) is nearly the same as that ratio in the L2000-like runs (1275 m/250 m = 5.1) and the ratio of the square roots of the two K ($\sqrt{50/2} = 5$). Similar agreements are found with the peak v component. However, in both L2000- and L6000-like runs, large differences in w_{max} are seen between the two constant K runs, with much weaker ascent obtained with $K = 2$ m^2 s^{-1}. A comparison of the runs

[3] The same symbol for the maximum value of a variable (e.g. u_{max}) is used to represent both the maximum value at a given time and the maximum value over the wave period. It should be clear from the context which type of maximum is being considered.

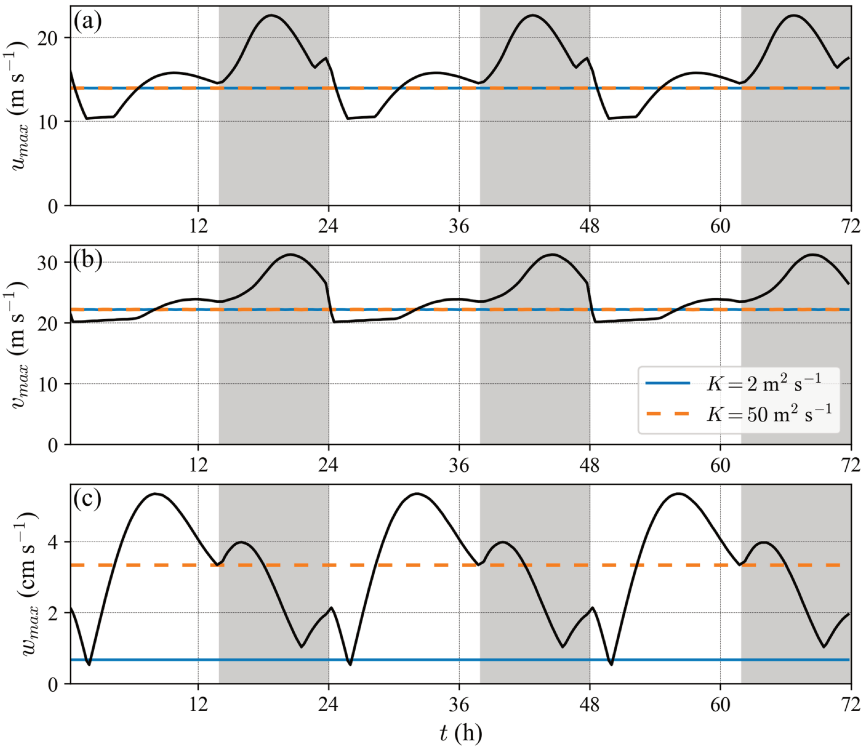

FIG. 7. Time series of u, v, and w maxima from experiment L2000: (a) $u_{\max}$ (m s^{-1}), (b) $v_{\max}$ (m s^{-1}), and (c) $w_{\max}$ (cm s^{-1}). Also shown are results from L2000-like experiments with no diurnal variations (K is constant); solid blue lines for $K = 2$ m^2 s^{-1}, and dashed orange lines for $K = 50$ m^2 s^{-1}. The maxima are the largest values in the analysis domain (one wavelength, from ground to $z = 10$ km).

with and without diurnal variations in K shows large increases in $u_{\max}$, $v_{\max}$, and $w_{\max}$ when diurnal variations are taken into account.

The dependence of $u_{\max}$, $v_{\max}$, and $w_{\max}$ on latitude is shown in Fig. 9 for L2000- and L6000-like experiments. While there is relatively little change in $u_{\max}$ or $v_{\max}$ with latitude, $w_{\max}$ does peak at the critical latitudes predicted in (83) (see also Fig. 1) for $j = -1$ and $j = 1$, particularly for $L = 2000$ km. Figure 9 also presents results from runs in which the Rayleigh damping parameter is reduced to (30 day)$^{-1}$. For both wavelengths, the $u_{\max}$ and $v_{\max}$ in the 30-day damping runs are nearly the same as in the 5-day damping runs for all latitudes. However, while $w_{\max}$ in the 30- and 5-day damping runs are similar for most latitudes, in the 30-day damping runs there is a marked increase in $w_{\max}$ on approach to the $j = -1$ and $j = 1$ critical latitudes, particularly for the $L = 2000$ km runs. Indeed, $w_{\max}$ at the critical latitude of 32.8°N is ≈8.0 cm s^{-1} with 5-day damping but ≈12.0 cm s^{-1} with 30-day damping.

The seemingly paradoxical result that $w_{\max}$ peaks at the $j = -1$ and $j = 1$ critical latitudes despite little change in $u_{\max}$ can be explained by examining the vertical extent of the disturbed winds (wind deviations) at different latitudes. We define a wind deviation depth scale h as the height at which u differs from its remote value by 2 m s^{-1} (in an rms sense). In other words, with $u_{\rm dev}(z)$ defined by

$$u_{\rm dev}(z) \equiv \sqrt{\frac{1}{\tau L}\int_0^{\tau}\int_0^{L} [u(x,z,t) - U]^2 dx\, dt}, \tag{98}$$

h is implicitly defined by

$$u_{\rm dev}(h) \equiv 2 \text{ m s}^{-1}. \tag{99}$$

This wind deviation depth scale[4] is plotted as a function of latitude for L2000- and L6000-like experiments with both 5- and 30-day damping rates in Fig. 10. In the 5-day damping runs with $L = 2000$ km, h attains a broad maximum (plateau) between the critical latitudes (see Fig. 1) of 27.1° and 32.8°N, while in the runs with $L = 6000$ km, local maxima in h emerge at the critical latitudes of 21.1° and 38.2°N. However, in the 30-day damping runs, pronounced maxima in h appear at all

[4] The analogous v-based depth scale h differed from this u-based scale by <200 m for $L = 2000$ km and by <450 m for $L = 6000$ km for latitudes between 15° and 50°N.

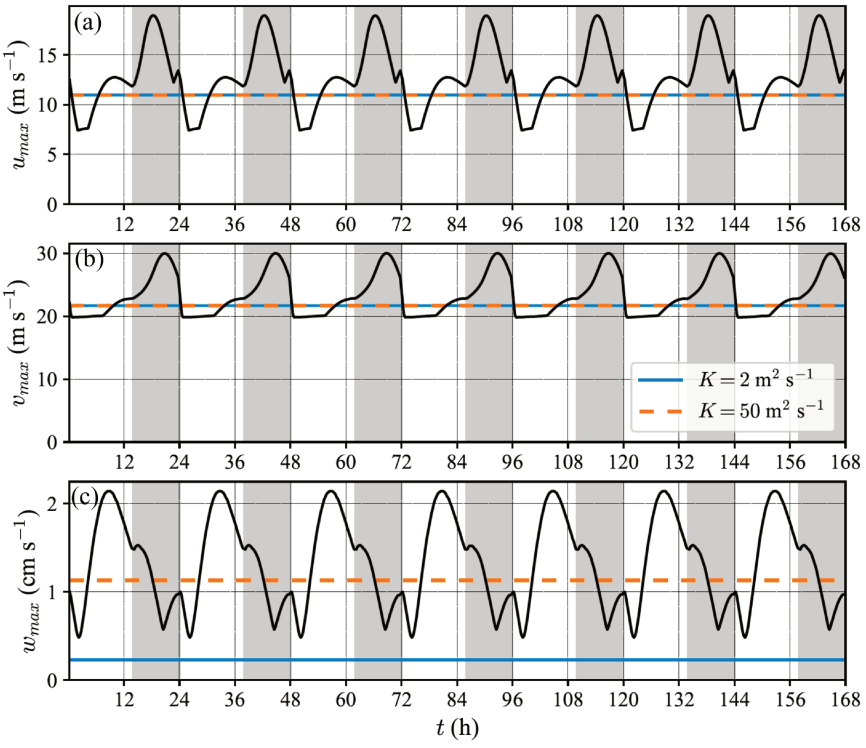

FIG. 8. As in Fig. 7, but for experiment L6000. Tick mark intervals/labels differ from those in Fig. 7.

three critical latitudes for both wavelengths. Thus, although the peak horizontal convergence is relatively independent of latitude ($u_{\max}$ is largely independent of latitude and the horizontal length scale is set by L), the convergence spans a greater depth (larger h) of the atmospheric column at the $j = -1$ and $j = 1$ critical latitudes. The vertical integral of the convergence (which yields w) is therefore largest at these latitudes. There is no tendency for an increase in $w_{\max}$ at the $j = 0$ critical latitude since the flow associated with $j = 0$ is nondivergent.

Time series of u, v, and w in L2000-like experiments at the 32.82°N critical latitude and a latitude just ~3° away (36°N) are shown on the $z = 5$ km surface for cases of 5- and 30-day damping in Fig. 11. The differences between the velocity components in the 5- and 30-day damping runs are much larger at 32.82°N than at 36°N. The amplitude of the w-oscillation and the peak value of w in the 30-day damping runs is much larger at 32.82°N; from $t = 34$ h to $t = 40$ h and from $t = 54$ h to $t = 62$ h, w is over 3 cm s^{-1} larger (40%–50% greater) at 32.82°N than at 36°N. Discrepancies between the v fields at the two latitudes exceed 5 m s^{-1} but appear to be more associated with a phase shift than an amplification.

Time–height plots of w at different latitudes for both L2000- and L6000-like runs show that the daytime peak (local maximum) of w occurs increasingly later in the afternoon at successively lower latitudes until, at sufficiently small latitudes, the afternoon peak disappears. The nocturnal mode dominates south of the 32.8°N critical latitude for $L = 2000$ km and south of the 38.2°N critical latitude for $L = 6000$ km. This behavior can be seen in Fig. 12 for L2000-like runs at 50° and 30°N (cf. with Fig. 5c for 40°N).

Last, L2000- and L6000-like experiments were run to examine the sensitivity of the flow to the time of sunset at different latitudes. In the L2000-like runs, the changes in both $u_{\max}$ and $v_{\max}$ between an early sunset of $t_{\text{set}} = 11$ h and a late sunset of $t_{\text{set}} = 15$ h are less than 0.7 m s^{-1} (relative changes < 3%) throughout a 30° to 50°N latitude band. The corresponding relative changes in $w_{\max}$, although larger than the relative changes in $u_{\max}$ and $v_{\max}$, are still small. For example, at 30°N, $w_{\max}$ decreases from ≈7.9 cm s^{-1} when $t_{\text{set}} = 11$ h to ≈6.5 cm s^{-1} when $t_{\text{set}} = 15$ h (18% decrease), while at 50°N, the corresponding change in $w_{\max}$ is an increase from ≈3.9 to ≈4.6 cm s^{-1} (18% increase). Qualitatively similar relative changes in the wind and vertical velocity maxima are found in the L6000-like runs. Unsurprisingly, for both wavelengths, the winds and vertical velocity attain their nighttime maxima at roughly the same time relative to sunset and thus occur later with later sunsets. In cases where the overall peak vertical velocity occurs during the daytime, the time of the maximum also occurs later with later sunsets, but the shift is not as pronounced as for the nocturnal maximum (e.g., there is only a 1.4 h shift in the afternoon maximum in w from early to late sunsets at 30°N with $L = 6000$ km).

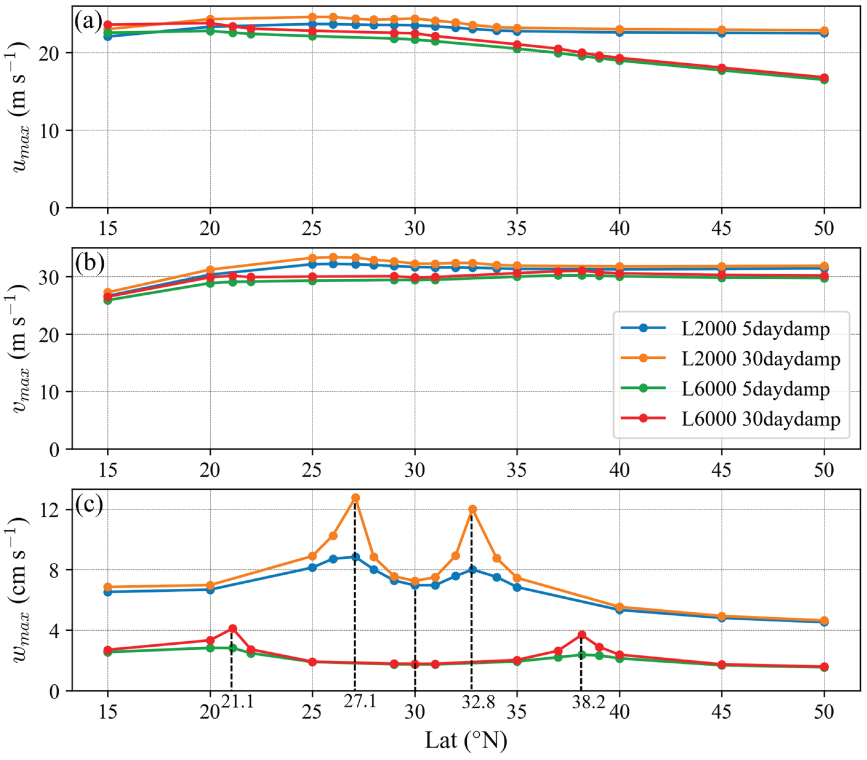

FIG. 9. The u, v, and w maxima as functions of latitude in experiments L2000 and L6000 and in related experiments in which the damping parameter R provides 30-day damping instead of 5-day damping: (a) $u_{\max}$ (m s^{-1}), (b) $v_{\max}$ (m s^{-1}), and (c) $w_{\max}$ (cm s^{-1}). Results are shown for (blue line) experiment L2000, (orange line) an L2000-like run with 30-day damping, (green line) experiment L6000, and (red line) an L6000-like run with 30-day damping. The maxima are the largest values in the analysis domain over one wave period. Dashed vertical lines in (c) mark the critical latitudes predicted by (83) (see also Fig. 1).

8. Summary and conclusions

The linkage between Rossby waves and extreme weather events, including heavy rainfall and flooding, is well established (Wirth et al. 2018). As convection is often impacted by conditions in the lower troposphere, we are motivated to study variations of wind and vertical velocity in the boundary layer during the passage of a zonally propagating Rossby wave. An analytical model is introduced to explore the spatial and temporal characteristics of NLLJs and ascent (Ekman pumping) in a diurnally varying frictional boundary layer during wave passage. The model combines the main aspects of the Ekman (1905), Åkerblom (1908) theories for frictional boundary layers on the rotating Earth, the Blackadar (1957) theory for NLLJs arising from inertial oscillations triggered by the shutdown of turbulence at sunset, and the Rossby (1939) theory for barotropic Rossby waves on a beta plane. The governing equations are the linearized Reynolds-averaged Boussinesq- and beta-plane-approximated horizontal equations of motion, the hydrostatic equation, and the incompressibility condition. The restrictions to a barotropic setting and a neutrally stratified environment are major limitations of our model. As in the slab and one-dimensional models of wind-induced Ekman layers in the upper ocean discussed in the introduction, our model includes Rayleigh damping terms to account for momentum damping associated with inertia–gravity waves that cannot be explicitly simulated. Since our model is restricted to the steady-periodic state, the Rossby wave period must be an integral number of days (diurnal frequency is a harmonic of the wave frequency). The governing equations are solved for eddy viscosities K that vary diurnally but are independent of height. We consider diurnally varying K with otherwise arbitrary time variations and K that vary as piecewise constant functions of time with step changes at sunrise and sunset. Flows of the latter type are explored for relatively short (L = 2000 km) and moderate (L = 6000 km) wavelengths. Additionally, these viscous flows are compared (at night) to flows obtained from an inviscid calculation. Among the model predictions are the following:

(i) NLLJ winds begin to develop at sunset, turn anticyclonically through the night, and reach peak strength a few hours after midnight. Such flows are consistent with the inviscid Blackadar (1957) IO mechanism for NLLJs, but are not pure IOs since our pressure gradient force varies in x and t. The magnitudes and locations of the peak u, v, and horizontal divergence fields from the viscous

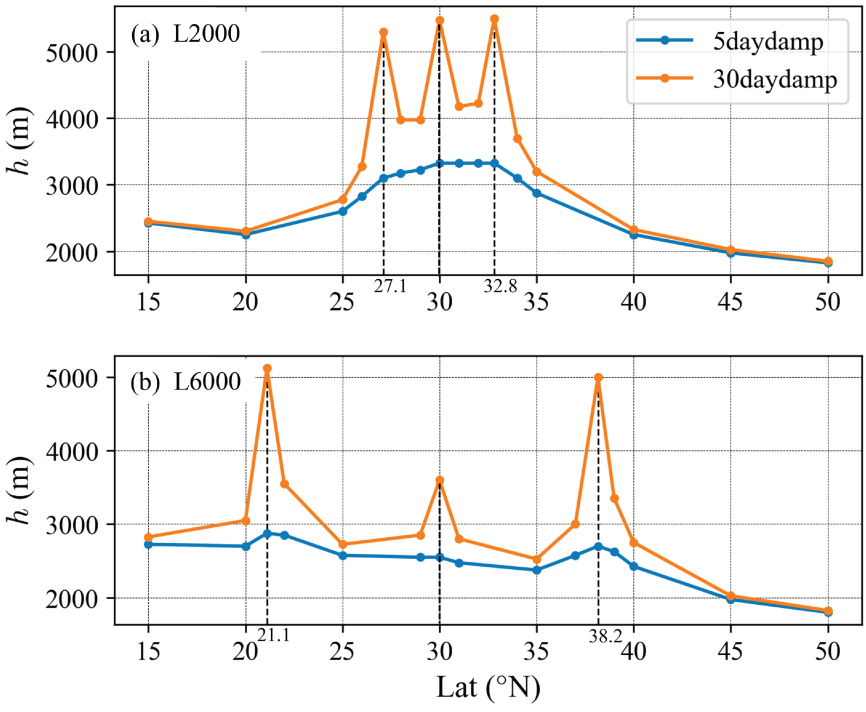

FIG. 10. Wind deviation depth scale h as a function of latitude in experiments (a) L2000 and (b) L6000. Also shown are results from experiments in which the damping parameter was adjusted to provide 30-day damping instead of 5-day damping: Blue lines depict results from experiments L2000 and L6000. Orange lines depict results from L2000- and L6000-like runs with 30-day damping. Dashed vertical lines mark the critical latitudes predicted by (83) (see also Fig. 1).

model are in good agreement with those from the inviscid calculation during the nighttime. The extrema in u and in the horizontal divergence of the wind field move with the westerly current.

(ii) There are two main modes of ascent: an elevated daytime mode and a lower-altitude nighttime mode. The nighttime mode is associated with a weak but persistent surge of convergent flow triggered by the shutdown of turbulence at sunset, the same mechanism that triggers IOs/NLLJs in the Blackadar model. The nocturnal surge is reminiscent of that predicted in Shapiro et al. (2018), although the inertia–gravity wave characteristics of the ascent in that study cannot be simulated in the present neutrally stratified model. The daytime peak w occurs increasingly later in the afternoon with decreasing latitude. South of critical latitudes (32.8°N for $L = 2000$ km and 38.2°N for $L = 6000$ km), the nighttime mode dominates. The model predicts that $w \propto kA$ for Rossby numbers $kU/f \ll 1$.

(iii) If the Rayleigh damping is turned off ($R = 0$), the model breaks down where (77) is satisfied, that is, where the inertial frequency, advection frequency (jkU; $j = -1, 0, 1$), and a harmonic of the wave frequency (of which the diurnal frequency is an integral multiple) sum to 0. This occurs at the three critical latitudes associated with $j = -1, 0, 1$ in (83) for the Northern Hemisphere. Corresponding to $j = 0$ is the 30°N diurnal-inertial resonant latitude noted in previous studies (see the introduction). The critical latitudes associated with $j = -1$ and $j = 1$ vary with wavelength. Breakdown is manifested as (i) u and v fields that do not approach their free-atmosphere profiles as $z \to \infty$ at the three critical latitudes, in violation of a remote boundary condition, and (ii) a vertical velocity that becomes infinite as $z \to \infty$ at the $j = -1$ and $j = 1$ critical latitudes. However, there is no prediction for u or v to peak at any critical latitude.

(iv) Breakdown cannot occur if $R \neq 0$. However, with both $R = (5 \text{ days})^{-1}$ and $R = (30 \text{ days})^{-1}$ damping, the peak w is found at the $j = -1$ and $j = 1$ critical latitudes. The effect is most pronounced for the run with shorter wavelength ($L = 2000$ km) and weaker damping [$R = (30 \text{ days})^{-1}$], where w increases from ≈ 4.5 cm s^{-1} at 50°N to ≈ 8.0 cm s^{-1} at the 32.8°N critical latitude. Additionally, a wind deviation depth scale h [defined via (98) and (99)] is significantly larger at the three critical latitudes for both $L = 2000$ km and $L = 6000$ km when the damping is weak [$R = (30 \text{ days})^{-1}$]; the response is muted for the more strongly damped case [$R = (5 \text{ days})^{-1}$]. The tendency for the depth scale to increase at the critical latitudes in the weakly damped case was reminiscent of

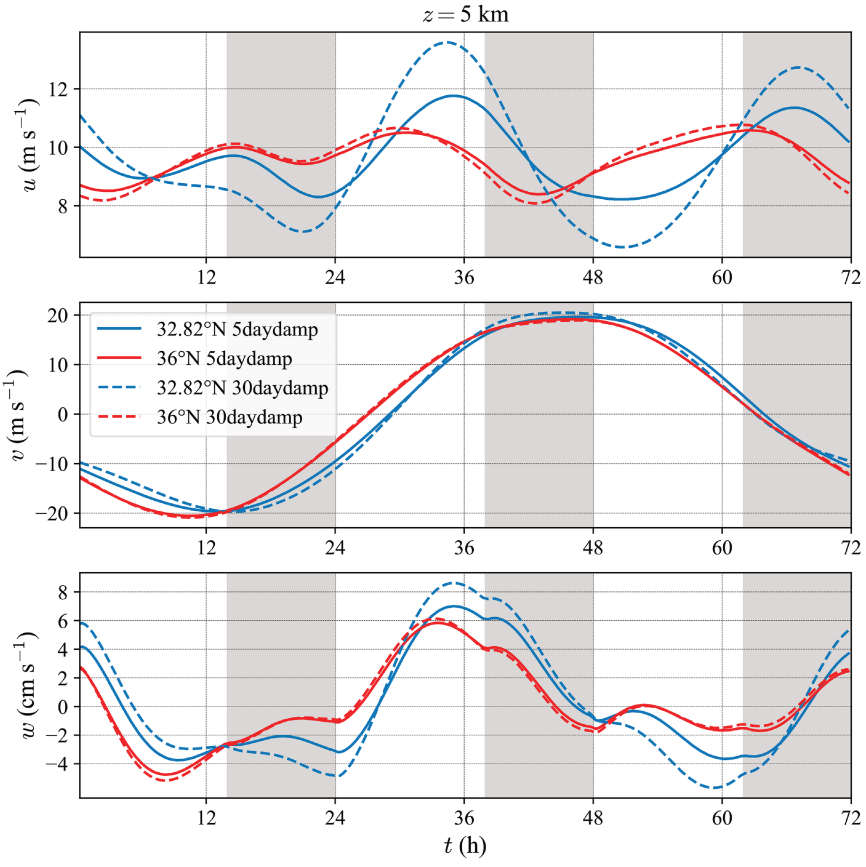

FIG. 11. Time series of (a) u (m s^{-1}), (b) v (m s^{-1}), and (c) w (cm s^{-1}) at $z = 5$ km at the x locations of their respective domain-wide maxima (though only the x location of nighttime maximum is considered for w). Results are shown for L2000-like runs at the 32.82°N critical latitude (blue lines) and at 36°N (red lines) for 5-day damping (solid lines) and 30-day damping (dashed lines).

the increased upper-ocean mixed layer depths at the 30°N critical latitude for diurnal-inertial resonance documented in the oceanographic literature (e.g., Zhang et al. 2010; Ashkenazy 2017; Vincze et al. 2019). In contrast to those studies, however, no discernible increases in our model u or v fields were found in the vicinity of any critical latitude; for $L = 2000$ km, u and v are remarkably uniform across a 20°–50°N latitude band while, for $L = 6000$ km, v is again nearly uniform across that band but u decreases northward, a trend consistent with the northward decrease in U required by the dispersion relation (see Table 2).

The vertical velocities predicted by our diurnally varying Ekman-Rossby model, particularly for the waves of smaller wavelength ($L = 2000$ km), can plausibly play a role in the initiation or maintenance of deep convection. Our study was motivated by questions about the nocturnal convection maximum observed during the warm season over the Great Plains. In this context, the ascent after sunset may facilitate the intensification or persistence of eastward-propagating convection that initiated during the afternoon over higher terrain to the west. However, without provision for an ambient stratification, the model's vertical velocities are likely overestimates (no lid effect) and it is not possible to study any direct role of inertia–gravity waves in countering a resonant response. As our analytical model framework cannot be extended to include stratification (via a thermal energy equation) since separable solutions are not possible for that case, numerical model simulations may be the best tool to explore the more realistic stratified problem. Numerical simulations can also be used to explore possible synergies between the ascent mechanism described in this paper and ascent associated with warm tongues or other surface-based thermal inhomogeneities typically found over the Great Plains, and the extent to which the combined effects increase the likelihood for deep convection.

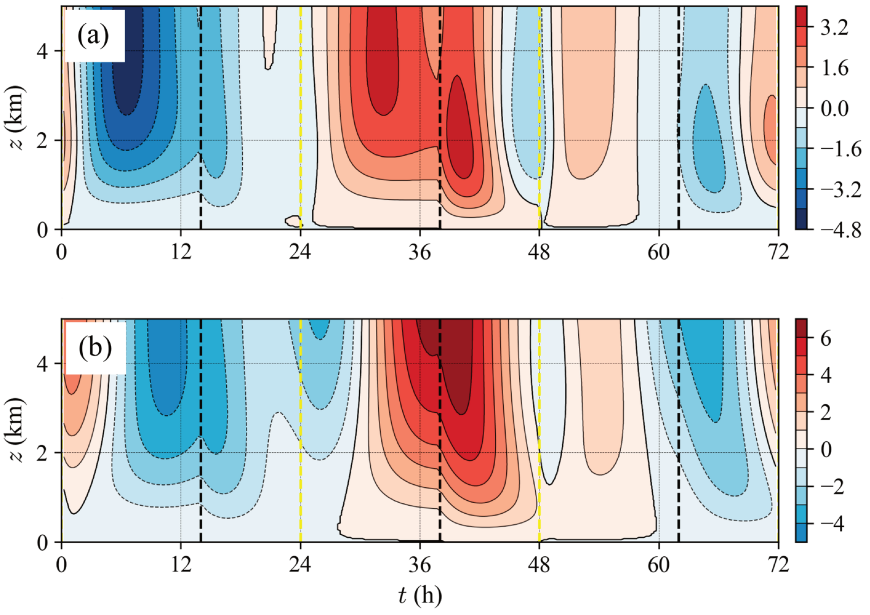

FIG. 12. Time–height plots of w (cm s^{-1}) through the x locations of their nocturnal maxima for L2000-like runs at (a) 50° and (b) 30°N; see Fig. 5c for the 40°N plot. Thick dashed yellow and black lines indicate times of sunrise and sunset, respectively. Note the differences between color bars.

Acknowledgments. This research was supported by NSF AGS-1921587. This paper has benefited greatly from the many helpful comments of the anonymous referees. We also thank Hristo Chipilski for his comments on an earlier presentation on this topic. Shawn Riley and David Goines provided computer assistance.

Data availability statement. The analytical model is available from the lead author upon request.

APPENDIX A

List of Symbols

Table A1 provides a list of symbols used in the article.

TABLE A1. Symbols, their descriptions, and first numbered equations in which they appear (definitions usually given nearby). If a symbol does not appear in any numbered equation, the section where it is first used is noted.

Symbol	Description	First numbered equation
a	Mean radius of Earth	(4)
A	Amplitude of Rossby wave (v component)	(12)
A_j, B_j, C_j	Constants in solutions for Z_j and T_j	(57), (58)
b_{jm}, c_{jm}, d_{jm}	Constants in evaluation of Φ_{jm}	(91)
D_j	Constants in solution for P_j	(59)
D_{jm}	Extended D_j constants (summation over m)	(63)
DAY	Union of daytime intervals in one wave period	(84)
E_j	Constants in solution for D_{jm}	(73)
f	Coriolis parameter (inertial frequency)	(1)
F_m	Functions of time in solution for P_j	(63)
h	Wind deviation depth scale	(99)
H	A function of $x - Ut$ in inviscid solution for Q	(34)
i	Imaginary unit; $i = \sqrt{-1}$	(25)
$\Im()$	Imaginary part	(31)
j	Index for the three parts ($j = -1, 0, 1$) of solution for Q	(49)
k	Wavenumber; $k = 2\pi/L$	(12)
K	Eddy viscosity	(1), (2)
$\overline{K}$	Average of K over wave period	(60)
K_d, K_n	Eddy viscosities during the day and night, respectively	(84)
l	Integer constant in equation for inviscid δ extrema	(43)
L	Wavelength	(7)
m	Index for m summation, generalizes λ_j to λ_{jm}	(62)
n	Integer constant in equation for inviscid u extrema	(41)
N	Day number	(85), (86)
N_τ	Number of days in wave period	(16)

TABLE A1. (*Continued*)

Symbol	Description	First numbered equation
NIGHT	Union of nighttime intervals in one wave period	(84)
p	Pressure	Section 2a
p_r	Pressure in reference state	Section 2a
p_{jm}	Constants in evaluation of Φ_{jm}	(95)
P_j	Time and height dependent parts of Q	(48)
q	Integer constant in equation for inviscid v extrema	(45), (C8)
Q	Complex wind deviation	(25)
Q_1, Q_2	Two hypothetical solutions for Q	Appendix B
Q_d	Difference between two hypothetical solutions for Q	(B1)
r_{jm}	Constants in polar form of λ_{jm}	(67)
R	Rayleigh damping constant	(1), (2)
$\Re()$	Real part	(31)
sgnω	Unit sign function; sgn$\omega \equiv -1$, 0, 1 for $\omega < 0$, $\omega = 0$, $\omega > 0$	(17)
t	Time	(1), (2)
t_{24}	24 h	(16)
t_{set}	Time of first sunset (hours after first sunrise)	(85), (86)
$t_{N\text{set}}$	Time of sunset on $(N + 1)$th day (hours after first sunrise)	(35)
T_j	Time-dependent part of P_j	(53)
u, v, w	x-, y-, and z-components of velocity	(1)–(3)
u_{dev}	Root-mean-square deviation of u from u_∞, a function of z	(98)
u_g, v_g	x- and y- components of geostrophic wind	(22)
$u_{\max}$, $v_{\max}$, $w_{\max}$	Maxima (with respect to x) of u, v, and w	Section 7
u_{peak}, v_{peak}	Maxima (with respect to x) of u and v in inviscid solution	(42), (46)
u_∞, v_∞	Remote ($z \to \infty$) u, v velocity components	(1), (2)
U	Westerly current speed	(1), (2)
x, y, z	Cartesian coordinates; east (x), north (y), up (z)	(1)–(3)
x_u, x_{div}, x_v	Locations of inviscid u, δ, v extrema	(41), (43), (45)
$z_{u\max}$, $z_{v\max}$	Heights of maxima (with respect to x) of u and v	Section 7
z_{low}	Low altitude where a nocturnal low-level jet forms	(35)
Z_j	Height-dependent part of P_j	(53)
β	Rossby parameter; $\beta \equiv df/dy$	(4)
Γ	Function of time in inviscid solution for v_{peak}	(46), (47)
δ	Horizontal divergence of wind field	(40)
δ_{peak}	Peak horizontal divergence of wind field in inviscid solution	(44)
δ_{mn}	Kronecker delta	(66)
ϵ	Wind fraction parameter in inviscid solution	(35)
ζ_∞	Remote ($z \to \infty$) vertical vorticity	(10)
θ_{jm}	Constants in polar form of λ_{jm}	(67)

TABLE A1. (*Continued*)

Symbol	Description	First numbered equation
κ	Function of time; $\kappa(t) \equiv (1/\overline{K})\int_0^t K(t')dt'$	(63)
λ_j	Separation constants in equations for T_j and Z_j	(55), (56)
λ_{jm}	Extended λ_j constants (summation over m)	(62)
μ	Time-dependent phase shift in location of inviscid v extrema	(C3)
$\hat{\mu}$	Function of time related to μ; $\mu = \hat{\mu} + \pi$	(C6), (C7)
Π	Kinematic pressure perturbation	(1), (2)
ρ_r	Constant reference density	Section 2a
τ	Wave period	(15)
Φ_{jm}	Time-dependent functions whose integrals contribute to D_{jm}	(89)
ϕ	Latitude	(4)
ϕ_c	Critical latitude	(83)
ψ_∞	Remote ($z \to \infty$) streamfunction	(11)
Ω	Angular velocity of Earth (diurnal frequency)	(4)
ω	Rossby wave frequency	(12)

APPENDIX B

Uniqueness Proof

A variant of the energy method (Gustafson 1987) shows that if a solution of (25) subject to (27)–(30) exists, it is unique. If Q_1 and Q_2 satisfy (25), their difference, $Q_d \equiv Q_1 - Q_2$, satisfies

$$\frac{\partial Q_d}{\partial t} + U\frac{\partial Q_d}{\partial x} = -(R + if)Q_d + K(t)\frac{\partial^2 Q_d}{\partial z^2}, \tag{B1}$$

and the complex conjugate of their difference, Q_d^*, satisfies

$$\frac{\partial Q_d^*}{\partial t} + U\frac{\partial Q_d^*}{\partial x} = -(R - if)Q_d^* + K(t)\frac{\partial^2 Q_d^*}{\partial z^2}. \tag{B2}$$

Taking $Q_d^* \times$ (B1) + $Q_d \times$ (B2) [noting $|Q_d| = \sqrt{Q_d Q_d^*}$ and $Q_d\partial^2 Q_d^*/\partial z^2 = (\partial/\partial z)(Q_d\partial Q_d^*/\partial z) - (\partial Q_d/\partial z)(\partial Q_d^*/\partial z)$] yields

$$\frac{\partial |Q_d|^2}{\partial t} + U\frac{\partial |Q_d|^2}{\partial x} = -R|Q_d|^2 + K(t)\frac{\partial^2 |Q_d|^2}{\partial z^2} - 2K(t)\left|\frac{\partial Q_d}{\partial z}\right|^2. \tag{B3}$$

Since Q_1 and Q_2 also satisfy (27)–(30), Q_d satisfies $\lim_{z\to\infty} Q_d = 0$, $Q_d|_{x=0} = Q_d|_{x=L}$, $Q_d|_{z=0} = 0$, and $Q_d|_{t=0} = Q_d|_{t=\tau}$, as does $|Q_d|$. Integration of (B3) with respect to t over one wave period, x over one wavelength, and z from the ground to infinity, then yields

$$\int_0^\tau \int_0^L \int_0^\infty \left[R|Q_d|^2 + 2K(t)\left|\frac{\partial Q_d}{\partial z}\right|^2\right] dt\, dx\, dz = 0. \tag{B4}$$

Since $R > 0$, $K(t) > 0$, $|Q_d|^2 \geq 0$, and $|\partial Q_d/\partial z|^2 \geq 0$, (B4) can only be satisfied if Q_d is identically zero. Thus, $Q_1 = Q_2$, and the solution is unique.

APPENDIX C

Inviscid v Extrema

From (39), with (13) used for ω, we see that $\partial v/\partial x = 0$ at points $x = x_v(t)$ for which

$$\cos[k(x_v - Ut) + \beta t/k] - (1 - \epsilon)\cos[f(t - t_{N\text{set}})]\cos[k(x_v - Ut) + \beta t_{N\text{set}}/k] = 0. \tag{C1}$$

To find $x_v(t)$, expand the two cosines in (C1) containing x_v using the addition formula $\cos(a + b) = \cos a \cos b - \sin a \sin b$, with $a \equiv k(x_v - Ut)$ and b evident as a remainder, obtaining

$$\cos[k(x_v - Ut)]\{\cos(\beta t/k) - (1 - \epsilon)\cos[f(t - t_{N\text{set}})] \times \cos(\beta t_{N\text{set}}/k)\} - \sin[k(x_v - Ut)]\{\sin(\beta t/k) - (1 - \epsilon)\cos[f(t - t_{N\text{set}})]\sin(\beta t_{N\text{set}}/k)\} = 0. \tag{C2}$$

This can be written more succinctly as

$$\Gamma(t)\cos[k(x_v - Ut) + \mu(t)] = 0, \tag{C3}$$

where $\Gamma(>0)$ is defined in (47), and $\mu(t)$ satisfies

$$\cos\mu = \frac{1}{\Gamma}\left\{\cos\left(\frac{\beta t}{k}\right) - (1 - \epsilon)\cos[f(t - t_{N\text{set}})]\cos\left(\frac{\beta t_{N\text{set}}}{k}\right)\right\}, \tag{C4}$$

$$\sin\mu = \frac{1}{\Gamma}\left\{\sin\left(\frac{\beta t}{k}\right) - (1 - \epsilon)\cos[f(t - t_{N\text{set}})]\sin\left(\frac{\beta t_{N\text{set}}}{k}\right)\right\}. \tag{C5}$$

The signs of $\cos\mu$ and $\sin\mu$ inferred from (C4) and (C5) determine whether μ is in quadrant 1 ($\cos\mu > 0$, $\sin\mu > 0$), 2 ($\cos\mu < 0$, $\sin\mu > 0$), 3 ($\cos\mu < 0$, $\sin\mu < 0$), or 4 ($\cos\mu > 0$, $\sin\mu < 0$). Since the principal values of the inverse cosine are in quadrants 1 or 2, and the principal values of the inverse sine are in quadrants 1 or 4, we can get μ from the inverse cosine of (C4) if μ is in quadrants 1 or 2, and from the inverse sine of (C5) if μ is in quadrants 1 or 4. If μ is in quadrant 3, write $\mu = \hat{\mu} + \pi$, where $\hat{\mu}$ is in quadrant 1, multiply (C4) and (C5) by -1, and expand out $\cos(\hat{\mu} + \pi)$ and $\sin(\hat{\mu} + \pi)$. We thus obtain

$$\cos\hat{\mu} = \left|\frac{1}{\Gamma}\left\{\cos\left(\frac{\beta t}{k}\right) - (1 - \epsilon)\cos[f(t - t_{N\text{set}})]\cos\left(\frac{\beta t_{N\text{set}}}{k}\right)\right\}\right|, \tag{C6}$$

$$\sin\hat{\mu} = \left|\frac{1}{\Gamma}\left\{\sin\left(\frac{\beta t}{k}\right) - (1 - \epsilon)\cos[f(t - t_{N\text{set}})]\sin\left(\frac{\beta t_{N\text{set}}}{k}\right)\right\}\right|, \tag{C7}$$

whose inverses (either one) yield $\hat{\mu}$.

Since $\Gamma > 0$, the cosine in (C3) is zero, and its argument must be equal to $\pi/2 + q\pi$, where q is an integer. We thus obtain $x_v(t)$ as

$$x_v = Ut - \frac{\mu(t)}{k} + \frac{\pi}{k}\left(\frac{1}{2} + q\right). \tag{C8}$$

The peak values v_{peak} of v, obtained by evaluating (39) at $x = x_v$, with ω given by (13), are

$$v_{\text{peak}} = (1 - \epsilon)U\sin[f(t - t_{N\text{set}})] + A\sin(\pi/2 + q\pi + \beta t/k - \mu) - (1 - \epsilon)A\cos[f(t - t_{N\text{set}})]\sin(\pi/2 + q\pi + \beta t_{N\text{set}}/k - \mu). \tag{C9}$$

Applying the addition formula $\sin(a + b) = \cos a \sin b + \sin a \cos b$ with $a \equiv \pi/2 + q\pi$ in (C9) yields

$$v_{\text{peak}} = (1 - \epsilon)U\sin[f(t - t_{N\text{set}})] + (-1)^q A\cos(\beta t/k - \mu) + (-1)^{q+1}(1 - \epsilon)A\cos[f(t - t_{N\text{set}})]\cos(\beta t_{N\text{set}}/k - \mu). \tag{C10}$$

Using the addition formula for cosines to expand the two cosine terms in (C10) in which μ appears, followed by use of (C4) and (C5) for $\cos\mu$ and $\sin\mu$, respectively, yields

$$v_{\text{peak}} = (1 - \epsilon)U\sin[f(t - t_{N\text{set}})] + \frac{(-1)^q A}{\Gamma} \times \{1 + (1 - \epsilon)^2\cos^2[f(t - t_{N\text{set}})] - 2(1 - \epsilon)\cos[f(t - t_{N\text{set}})]\cos[\beta(t - t_{N\text{set}})/k]\}. \tag{C11}$$

In view of (47), (C11) reduces to

$$v_{\text{peak}} = (1 - \epsilon)U\sin[f(t - t_{N\text{set}})] + (-1)^q\Gamma A. \tag{C12}$$

REFERENCES

Agee, E. M., D. E. Brown, T. S. Chen, and K. E. Dowell, 1973: A height-dependent model of eddy viscosity in the planetary boundary layer. *J. Appl. Meteor.*, **12**, 409–412, https://doi.org/10.1175/1520-0450(1973)012<0409:AHDMOE>2.0.CO;2.

Åkerblom, F., 1908: Rechercher sur les courants le plus bas de l'atmosphere au-dessus de Paris. *Nova Acta Regiae Soc. Sci. Ups.*, **2**, 203–251.

Ashkenazy, Y., 2017: Energy transfer of surface wind-induced currents to the deep ocean via resonance with the Coriolis force. *J. Mar. Syst.*, **167**, 93–104, https://doi.org/10.1016/j.jmarsys.2016.11.019.

Baas, P., F. C. Bosveld, H. Klein Baltink, and A. A. M. Holtslag, 2009: A climatology of nocturnal low-level jets at Cabauw. *J. Appl. Meteor. Climatol.*, **48**, 1627–1642, https://doi.org/10.1175/2009JAMC1965.1.

Banta, R. M., R. K. Newsom, J. K. Lundquist, Y. L. Pichugina, R. L. Coulter, and L. Mahrt, 2002: Nocturnal low-level jet characteristics over Kansas during CASES-99. *Bound.-Layer Meteor.*, **105**, 221–252, https://doi.org/10.1023/A:1019992330866.

Blackadar, A. K., 1957: Boundary layer wind maxima and their significance for the growth of nocturnal inversions. *Bull.*

Amer. Meteor. Soc., **38**, 283–290, https://doi.org/10.1175/1520-0477-38.5.283.

Bonner, W. D., 1966: Case study of thunderstorm activity in relation to the low-level jet. *Mon. Wea. Rev.*, **94**, 167–178, https://doi.org/10.1175/1520-0493(1966)094<0167:CSOTAI>2.3.CO;2.

——, 1968: Climatology of the low level jet. *Mon. Wea. Rev.*, **96**, 833–850, https://doi.org/10.1175/1520-0493(1968)096<0833:COTLLJ>2.0.CO;2.

——, S. Esbensen, and R. Greenberg, 1968: Kinematics of the low-level jet. *J. Appl. Meteor.*, **7**, 339–347, https://doi.org/10.1175/1520-0450(1968)007<0339:KOTLLJ>2.0.CO;2.

Buajitti, K., and A. K. Blackadar, 1957: Theoretical studies of diurnal wind-structure variations in the planetary boundary layer. *Quart. J. Roy. Meteor. Soc.*, **83**, 486–500, https://doi.org/10.1002/qj.49708335804.

Carbone, R. E., and J. D. Tuttle, 2008: Rainfall occurrence in the U.S. warm season: The diurnal cycle. *J. Climate*, **21**, 4132–4146, https://doi.org/10.1175/2008JCLI2275.1.

Carroll, B. J., B. B. Demoz, and R. Delgado, 2019: An overview of low-level jet winds and corresponding mixed layer depths during PECAN. *J. Geophys. Res. Atmos.*, **124**, 9141–9160, https://doi.org/10.1029/2019JD030658.

Chereskin, T. K., 1995: Direct evidence for an Ekman balance in the California Current. *J. Geophys. Res.*, **100**, 18 261–18 269, https://doi.org/10.1029/95JC02182.

Constantin, A., and R. S. Johnson, 2019: Atmospheric Ekman flows with variable eddy viscosity. *Bound.-Layer Meteor.*, **170**, 395–414, https://doi.org/10.1007/s10546-018-0404-0.

Craig, P. D., 1989: A model of diurnally forced vertical current structure near 30° latitude. *Cont. Shelf Res.*, **9**, 965–980, https://doi.org/10.1016/0278-4343(89)90002-2.

Dai, A., F. Giorgi, and K. E. Trenberth, 1999: Observed and model-simulated diurnal cycles of precipitation over the contiguous United States. *J. Geophys. Res.*, **104**, 6377–6402, https://doi.org/10.1029/98JD02720.

Dandou, A., M. Tombrou, K. Schäfer, S. Emeis, A. P. Protonotariou, E. Bossioli, N. Soulakellis, and P. Suppan, 2009: A comparison between modelled and measured mixing-layer height over Munich. *Bound.-Layer Meteor.*, **131**, 425–440, https://doi.org/10.1007/s10546-009-9373-7.

D'Asaro, E. A., 1985: The energy flux from the wind to near-inertial motions in the surface mixed layer. *J. Phys. Oceanogr.*, **15**, 1043–1059, https://doi.org/10.1175/1520-0485(1985)015<1043:TEFFTW>2.0.CO;2.

——, C. C. Eriksen, M. D. Levine, C. A. Paulson, P. Niiler, and P. V. Meurs, 1995: Upper-ocean inertial currents forced by a strong storm. Part I: Data and comparisons with linear theory. *J. Phys. Oceanogr.*, **25**, 2909–2936, https://doi.org/10.1175/1520-0485(1995)025<2909:UOICFB>2.0.CO;2.

Defant, F., 1949: Zur theorie der Hangwinde, nebst Bemerkungen zur theorie der Berg- und Talwinde. *Arch. Meteor. Geophys. Bioklimatol.*, **A1**, 421–450, https://doi.org/10.1007/BF02247634.

Easterling, D. R., and P. J. Robinson, 1985: The diurnal variation of thunderstorm activity in the United States. *J. Climate Appl. Meteor.*, **24**, 1048–1058, https://doi.org/10.1175/1520-0450(1985)024<1048:TDVOTA>2.0.CO;2.

Ekman, V. W., 1905: On the influence of the Earth's rotation on ocean-currents. *Arch. Math. Astron. Phys.*, **2** (11), 1–52.

Fearon, G., S. Herbette, J. Veitch, G. Cambon, A. J. Lucas, F. Lemarié, and M. Vichi, 2020: Enhanced vertical mixing in coastal upwelling systems driven by diurnal-inertial resonance: Numerical experiments. *J. Geophys. Res. Oceans*, **125**, e2020JC016208, https://doi.org/10.1029/2020JC016208.

Gebauer, J. G., A. Shapiro, E. Fedorovich, and P. Klein, 2018: Convection initiation caused by heterogeneous low-level jets over the Great Plains. *Mon. Wea. Rev.*, **146**, 2615–2637, https://doi.org/10.1175/MWR-D-18-0002.1.

Gough, M. K., A. J. H. M. Reniers, J. H. MacMahan, and S. D. Howden, 2016: Resonant near-surface inertial oscillations in the northeastern Gulf of Mexico. *J. Geophys. Res. Oceans*, **121**, 2163–2182, https://doi.org/10.1002/2015JC011372.

Grachev, A. A., C. W. Fairall, P. O. G. Persson, E. L. Andreas, and P. S. Guest, 2005: Stable boundary-layer scaling regimes: The SHEBA data. *Bound.-Layer Meteor.*, **116**, 201–235, https://doi.org/10.1007/s10546-004-2729-0.

Grazzini, F., G. Fragkoulidis, F. Teubler, V. Wirth, and G. C. Craig, 2021: Extreme precipitation events over northern Italy. Part II: Dynamical precursors. *Quart. J. Roy. Meteor. Soc.*, **147**, 1237–1257, https://doi.org/10.1002/qj.3969.

Gustafson, K. E., 1987: *Introduction to Partial Differential Equations and Hilbert Space Methods*. 2nd ed. John Wiley and Sons, 409 pp.

Haurwitz, B., 1940: The motion of atmospheric disturbances. *J. Mar. Res.*, **3**, 35–50.

Hoskins, B. J., M. E. McIntyre, and A. W. Robertson, 1985: On the use and significance of isentropic potential vorticity maps. *Quart. J. Roy. Meteor. Soc.*, **111**, 877–946, https://doi.org/10.1002/qj.49711147002.

Hunkins, K., 1966: Ekman drift currents in the Arctic Ocean. *Deep-Sea Res.*, **13**, 607–620, https://doi.org/10.1016/0011-7471(66)90592-4.

Hyder, P., J. H. Simpson, J. Xing, and S. T. Gille, 2011: Observations over an annual cycle and simulations of wind-forced oscillations near the critical latitude for diurnal-inertial resonance. *Cont. Shelf Res.*, **31**, 1576–1591, https://doi.org/10.1016/j.csr.2011.06.001.

Ingel', L. K., 2015: One type of resonance phenomena in the atmosphere and water bodies. *Fluid Dyn.*, **50**, 494–500, https://doi.org/10.1134/S0015462815040043.

Jeričević, A., and Ž. Večenaj, 2009: Improvement of vertical diffusion analytic schemes under stable atmospheric conditions. *Bound.-Layer Meteor.*, **131**, 293–307, https://doi.org/10.1007/s10546-009-9367-5.

Jia, M., and Coauthors, 2019: Long-lived high-frequency gravity waves in the atmospheric boundary layer: Observations and simulations. *Atmos. Chem. Phys.*, **19**, 15 431–15 446, https://doi.org/10.5194/acp-19-15431-2019.

Jing, Z., L. Wu, and X. Ma, 2017: Energy exchange between the mesoscale oceanic eddies and wind-forced near-inertial oscillations. *J. Phys. Oceanogr.*, **47**, 721–733, https://doi.org/10.1175/JPO-D-16-0214.1.

Kallistratova, M. A., and R. D. Kouznetsov, 2012: Low-level jets in the Moscow region in summer and winter observed with a Sodar network. *Bound.-Layer Meteor.*, **143**, 159–175, https://doi.org/10.1007/s10546-011-9639-8.

Kim, S. Y., and G. Crawford, 2014: Resonant ocean current responses driven by coastal winds near the critical latitude. *Geophys. Res. Lett.*, **41**, 5581–5587, https://doi.org/10.1002/2014GL060402.

Kincer, J. B., 1916: Daytime and nighttime precipitation and their economic significance. *Mon. Wea. Rev.*, **44**, 628–633, https://doi.org/10.1175/1520-0493(1916)44<628:DANPAT>2.0.CO;2.

Kornhuber, K., D. Coumou, E. Vogel, C. Lesk, J. F. Donges, J. Lehmann, and R. M. Horton, 2020: Amplified Rossby waves enhance risk of concurrent heatwaves in major breadbasket

regions. *Nat. Climate Change*, **10**, 48–53, https://doi.org/10.1038/s41558-019-0637-z.

Kundu, P. K., 1976: An analysis of inertial oscillations observed near Oregon coast. *J. Phys. Oceanogr.*, **6**, 879–893, https://doi.org/10.1175/1520-0485(1976)006<0879:AAOIOO>2.0.CO;2.

Maas, L. R. M., and J. J. M. van Haren, 1987: Observations on the vertical structure of tidal and inertial currents in the central North Sea. *J. Mar. Res.*, **45**, 293–318, https://doi.org/10.1357/002224087788401106.

Maddox, R. A., 1983: Large-scale meteorological conditions associated with midlatitude mesoscale convective complexes. *Mon. Wea. Rev.*, **111**, 1475–1493, https://doi.org/10.1175/1520-0493(1983)111<1475:LSMCAW>2.0.CO;2.

Mahrt, L., and D. Vickers, 2006: Extremely weak mixing in stable conditions. *Bound.-Layer Meteor.*, **119**, 19–39, https://doi.org/10.1007/s10546-005-9017-5.

Mann, M. E., S. Rahmstorf, K. Kornhuber, B. A. Steinman, S. K. Miller, S. Petri, and D. Coumou, 2018: Projected changes in persistent extreme summer weather events: The role of quasi-resonant amplification. *Sci. Adv.*, **4**, eaat3272, https://doi.org/10.1126/sciadv.aat3272.

McWilliams, J. C., and E. Huckle, 2006: Ekman layer rectification. *J. Phys. Oceanogr.*, **36**, 1646–1659, https://doi.org/10.1175/JPO2912.1.

——, ——, and A. F. Shchepetkin, 2009: Buoyancy effects in a stratified Ekman layer. *J. Phys. Oceanogr.*, **39**, 2581–2599, https://doi.org/10.1175/2009JPO4130.1.

Means, L. L., 1952: On thunderstorm forecasting in the central United States. *Mon. Wea. Rev.*, **80**, 165–189, https://doi.org/10.1175/1520-0493(1952)080<0165:OTFITC>2.0.CO;2.

Mihanović, H., C. Pattiaratchi, and F. Verspecht, 2016: Diurnal sea breezes force near-inertial waves along Rottnest continental shelf, southwestern Australia. *J. Phys. Oceanogr.*, **46**, 3487–3508, https://doi.org/10.1175/JPO-D-16-0022.1.

Momen, M., and E. Bou-Zeid, 2017: Analytical reduced models for the non-stationary diabatic atmospheric boundary layer. *Bound.-Layer Meteor.*, **164**, 383–399, https://doi.org/10.1007/s10546-017-0247-0.

O'Brien, J. J., 1970: A note on the vertical structure of the eddy exchange coefficient in the planetary boundary layer. *J. Atmos. Sci.*, **27**, 1213–1215, https://doi.org/10.1175/1520-0469(1970)027<1213:ANOTVS>2.0.CO;2.

Oerlemans, J., 1998: The atmospheric boundary layer over melting glaciers. *Clear and Cloudy Boundary Layers*, A. A. M. Holtslag and P. G. Duynkerke, Eds., Royal Netherlands Academy of Arts and Sciences, 129–153.

Ooyama, K., 1957: A study of diurnal variation of wind caused by periodic variation of eddy viscosity. Final Rep. AF19(604)-1368, 80–135.

Paegle, J., and G. E. Rasch, 1973: Three-dimensional characteristics of diurnally varying boundary-layer flows. *Mon. Wea. Rev.*, **101**, 746–756, https://doi.org/10.1175/1520-0493(1973)101<0746:TCODVB>2.3.CO;2.

Papadopoulos, K. H., C. G. Helmis, A. T. Soilemes, J. Kalogiros, P. G. Papageorgas, and D. N. Asimakopoulos, 1997: The structure of katabatic flows down a simple slope. *Quart. J. Roy. Meteor. Soc.*, **123**, 1581–1601, https://doi.org/10.1002/qj.49712354207.

Parish, T. R., 2016: A comparative study of the 3 June 2015 Great Plains low-level jet. *Mon. Wea. Rev.*, **144**, 2963–2979, https://doi.org/10.1175/MWR-D-16-0071.1.

——, 2017: On the forcing of the summertime Great Plains low-level jet. *J. Atmos. Sci.*, **74**, 3937–3953, https://doi.org/10.1175/JAS-D-17-0059.1.

——, and R. D. Clark, 2017: On the initiation of the 20 June 2015 Great Plains low-level jet. *J. Appl. Meteor. Climatol.*, **56**, 1883–1895, https://doi.org/10.1175/JAMC-D-16-0187.1.

——, A. R. Rodi, and R. D. Clark, 1988: A case study of the summertime Great Plains low level jet. *Mon. Wea. Rev.*, **116**, 94–105, https://doi.org/10.1175/1520-0493(1988)116<0094:ACSOTS>2.0.CO;2.

——, R. D. Clark, and T. D. Sikora, 2020: Nocturnal destabilization associated with the summertime Great Plains low-level jet. *Mon. Wea. Rev.*, **148**, 4641–4656, https://doi.org/10.1175/MWR-D-19-0394.1.

Park, J. J., K. Kim, and R. W. Schmitt, 2009: Global distribution of the decay timescale of mixed layer inertial motions observed by satellite-tracked drifters. *J. Geophys. Res.*, **114**, C11010, https://doi.org/10.1029/2008JC005216.

Pedlosky, J., 1987: *Geophysical Fluid Dynamics*. 2nd ed. Springer-Verlag, 710 pp.

Pitchford, K. L., and J. London, 1962: The low-level jet as related to nocturnal thunderstorms over Midwest United States. *J. Appl. Meteor.*, **1**, 43–47, https://doi.org/10.1175/1520-0450(1962)001<0043:TLLJAR>2.0.CO;2.

Pollard, R. T., and R. C. Millard Jr., 1970: Comparison between observed and simulated wind-generated inertial oscillations. *Deep-Sea Res.*, **17**, 813–821, https://doi.org/10.1016/0011-7471(70)90043-4.

Price, J. F., and M. A. Sundermeyer, 1999: Stratified Ekman layers. *J. Geophys. Res.*, **104**, 20 467–20 494, https://doi.org/10.1029/1999JC900164.

——, R. A. Weller, and R. R. Schudlich, 1987: Wind-driven ocean currents and Ekman transport. *Science*, **238**, 1534–1538, https://doi.org/10.1126/science.238.4833.1534.

Reif, D. W., and H. B. Bluestein, 2017: A 20-year climatology of nocturnal convection initiation over the central and southern Great Plains during the warm season. *Mon. Wea. Rev.*, **145**, 1615–1639, https://doi.org/10.1175/MWR-D-16-0340.1.

Rhines, P. B., 2002: Rossby waves. *Encyclopedia of Atmospheric Sciences*, Elsevier, 1923–1939.

Rossby, C.-G., 1939: Relation between variations in the intensity of the zonal circulation of the atmosphere and the displacements of the semi-permanent centers of action. *J. Mar. Res.*, **2**, 38–55.

——, 1940: Planetary flow patterns in the atmosphere. *Quart. J. Roy. Meteor. Soc.*, **66**, 68–87.

Rysman, J.-F., A. Lahellec, E. Vignon, C. Genthon, and S. Verrier, 2016: Characterization of atmospheric Ekman spirals at Dome C, Antarctica. *Bound.-Layer Meteor.*, **160**, 363–373, https://doi.org/10.1007/s10546-016-0144-y.

Saffin, L., J. Methven, J. Bland, B. Harvey, and C. Sanchez, 2021: Circulation conservation in the outflow of warm conveyor belts and consequences for Rossby wave evolution. *Quart. J. Roy. Meteor. Soc.*, **147**, 3587–3610, https://doi.org/10.1002/qj.4143.

Shaffer, G., 1972: A theory of time-dependent upwelling induced by a spatially- and temporally-varying wind with emphasis on the effects of a seabreeze–landbreeze cycle. *Kiel. Meeresforsch.*, **28**, 139–161.

Shapiro, A., E. Fedorovich, and S. Rahimi, 2016: A unified theory for the Great Plains nocturnal low-level jet. *J. Atmos. Sci.*, **73**, 3037–3057, https://doi.org/10.1175/JAS-D-15-0307.1.

——, ——, and J. G. Gebauer, 2018: Mesoscale ascent in nocturnal low-level jets. *J. Atmos. Sci.*, **75**, 1403–1427, https://doi.org/10.1175/JAS-D-17-0279.1.

——, J. G. Gebauer, and D. B. Parsons, 2022: Emergence of a nocturnal low-level jet from a broad baroclinic zone. *J. Atmos. Sci.*, **79**, 1363–1383, https://doi.org/10.1175/JAS-D-21-0187.1.

Sharan, M., and S. G. Gopalakrishnan, 1997: Comparative evaluation of eddy exchange coefficients for strong and weak wind stable boundary layer modelling. *J. Appl. Meteor.*, **36**, 545–559, https://doi.org/10.1175/1520-0450(1997)036<0545:CEOEEC>2.0.CO;2.

Shibuya, R., K. Sato, and M. Nakanishi, 2014: Diurnal wind cycles forcing inertial oscillations: A latitude-dependent resonance phenomenon. *J. Atmos. Sci.*, **71**, 767–781, https://doi.org/10.1175/JAS-D-13-0124.1.

Simpson, J. H., P. Hyder, T. P. Rippeth, and I. M. Lucas, 2002: Forced oscillations near the critical latitude for diurnal-inertial resonance. *J. Phys. Oceanogr.*, **32**, 177–187, https://doi.org/10.1175/1520-0485(2002)032<0177:FONTCL>2.0.CO;2.

Song, J., K. Liao, R. L. Coulter, and B. M. Lesht, 2005: Climatology of the low-level jet at the southern Great Plains atmospheric boundary layer experiments site. *J. Appl. Meteor.*, **44**, 1593–1606, https://doi.org/10.1175/JAM2294.1.

Stockwell, R. G., W. G. Large, and R. F. Milliff, 2004: Resonant inertial oscillations in moored buoy ocean surface winds. *Tellus*, **56A**, 536–547, https://doi.org/10.3402/tellusa.v56i5.14478.

Stull, R. B., 1988: *An Introduction to Boundary Layer Meteorology*. Kluwer Academic, 666 pp.

Tan, Z.-M., and M. M. Farahani, 1998: An analytical study of the diurnal variations of wind in a semi-geostrophic Ekman boundary layer model. *Bound.-Layer Meteor.*, **86**, 313–332, https://doi.org/10.1023/A:1000694732459.

Tombrou, M., A. Dandou, C. Helmis, E. Akylas, G. Angelopoulos, H. Flocas, V. Assimakopoulos, and N. Soulakellis, 2007: Model evaluation of the atmospheric boundary layer and mixed-layer evolution. *Bound.-Layer Meteor.*, **124**, 61–79, https://doi.org/10.1007/s10546-006-9146-5.

Trier, S. B., and D. B. Parsons, 1993: Evolution of environmental conditions preceding the development of a nocturnal mesoscale convective complex. *Mon. Wea. Rev.*, **121**, 1078–1098, https://doi.org/10.1175/1520-0493(1993)121<1078:EOECPT>2.0.CO;2.

——, J. W. Wilson, D. A. Ahijevych, and R. A. Sobash, 2017: Mesoscale vertical motions near nocturnal convection initiation in PECAN. *Mon. Wea. Rev.*, **145**, 2919–2941, https://doi.org/10.1175/MWR-D-17-0005.1.

Tuttle, J. D., and C. A. Davis, 2006: Corridors of warm-season precipitation in the central United States. *Mon. Wea. Rev.*, **134**, 2297–2317, https://doi.org/10.1175/MWR3188.1.

Tyson, P. D., 1968: Velocity fluctuations in the mountain wind. *J. Atmos. Sci.*, **25**, 381–384, https://doi.org/10.1175/1520-0469(1968)025<0381:VFITMW>2.0.CO;2.

Vincze, M., N. Fenyvesi, M. Klein, J. Sommeria, S. Viboud, and Y. Ashkenazy, 2019: Evidence for wind-induced Ekman layer resonance based on rotating tank experiments. *Europhys. Lett.*, **125**, 44001, https://doi.org/10.1209/0295-5075/125/44001.

Wallace, J. M., 1975: Diurnal variations in precipitation and thunderstorm frequency over the conterminous United States. *Mon. Wea. Rev.*, **103**, 406–419, https://doi.org/10.1175/1520-0493(1975)103<0406:DVIPAT>2.0.CO;2.

Walters, C. K., and J. A. Winkler, 2001: Airflow configurations of warm season southerly low-level wind maxima in the Great Plains. Part I: Spatial and temporal characteristics and relationship to convection. *Wea. Forecasting*, **16**, 513–530, https://doi.org/10.1175/1520-0434(2001)016<0513:ACOWSS>2.0.CO;2.

——, ——, R. P. Shadboldt, J. van Ravensway, and G. D. Bierly, 2008: A long-term climatology of southerly and northerly low-level jets for the central United States. *Ann. Assoc. Amer. Geogr.*, **98**, 521–552, https://doi.org/10.1080/00045600802046387.

Watanabe, M., and T. Hibiya, 2002: Global estimates of the wind-induced energy flux to inertial motions in the surface mixed layer. *Geophys. Res. Lett.*, **29**, 1239, https://doi.org/10.1029/2001GL014422.

Weckwerth, T. M., and D. B. Parsons, 2006: A review of convection initiation and motivation for IHOP_2002. *Mon. Wea. Rev.*, **134**, 5–22, https://doi.org/10.1175/MWR3067.1.

——, J. Hanesiak, J. W. Wilson, S. B. Trier, S. K. Degelia, W. A. Gallus Jr., R. D. Roberts, and X. Wang, 2019: Nocturnal convection initiation during PECAN 2015. *Bull. Amer. Meteor. Soc.*, **100**, 2223–2239, https://doi.org/10.1175/BAMS-D-18-0299.1.

Weller, R. A., 1981: Observations of the velocity response to wind forcing in the upper ocean. *J. Geophys. Res.*, **86**, 1969–1977, https://doi.org/10.1029/JC086iC03p01969.

——, 1982: The relation of near-inertial motions observed in the mixed layer during the JASIN (1978) experiment to the local wind stress and to the quasi-geostrophic flow field. *J. Phys. Oceanogr.*, **12**, 1122–1136, https://doi.org/10.1175/1520-0485(1982)012<1122:TRONIM>2.0.CO;2.

Whiteman, C. D., X. Bian, and S. Zhong, 1997: Low-level jet climatology from enhanced rawinsonde observations at a site in the southern Great Plains. *J. Appl. Meteor.*, **36**, 1363–1376, https://doi.org/10.1175/1520-0450(1997)036<1363:LLJCFE>2.0.CO;2.

Whitt, D. B., and L. N. Thomas, 2015: Resonant generation and energetics of wind-forced near-inertial motions in a geostrophic flow. *J. Phys. Oceanogr.*, **45**, 181–208, https://doi.org/10.1175/JPO-D-14-0168.1.

Wilson, J. W., and R. D. Roberts, 2006: Summary of convective storm initiation and evolution during IHOP: Observational and modeling perspective. *Mon. Wea. Rev.*, **134**, 23–47, https://doi.org/10.1175/MWR3069.1.

Wirth, V., M. Riemer, E. K. M. Chang, and O. Martius, 2018: Rossby wave packets on the midlatitude waveguide—A review. *Mon. Wea. Rev.*, **146**, 1965–2001, https://doi.org/10.1175/MWR-D-16-0483.1.

Yamada, T., and G. Mellor, 1975: A simulation of the Wangara atmospheric boundary layer data. *J. Atmos. Sci.*, **32**, 2309–2329, https://doi.org/10.1175/1520-0469(1975)032<2309:ASOTWA>2.0.CO;2.

Zhang, X., S. F. DiMarco, D. C. Smith IV, M. K. Howard, A. E. Jochens, and R. D. Hetland, 2009: Near-resonant ocean response to sea breeze on a stratified continental shelf. *J. Phys. Oceanogr.*, **39**, 2137–2155, https://doi.org/10.1175/2009JPO4054.1.

——, D. C. Smith IV, S. F. DiMarco, and R. D. Hetland, 2010: A numerical study of sea-breeze-driven ocean Poincare wave propagation and mixing near the critical latitude. *J. Phys. Oceanogr.*, **40**, 48–66, https://doi.org/10.1175/2009JPO4216.1.

Zhong, S., J. D. Fast, and X. Bian, 1996: A case study of the Great Plains low-level jet using wind profiler network data and a high-resolution numerical model. *Mon. Wea. Rev.*, **124**, 785–806, https://doi.org/10.1175/1520-0493(1996)124<0785:ACSOTG>2.0.CO;2.